232 (2024) 212419

Contents lists available at ScienceDirect

Geoenergy Science and Engineering

journal homepage: www.sciencedirect.com/journal/geoenergy-science-and-engineering

Petrographic and geochemical characteristics of the Middle Devonian Eifelian Nabiao Formation in the Youjiang Basin, South China: Implications for paleoenvironment and organic matter accumulation mechanism

Yuzuo Liu [a,b], Wanzhong Shi [a,b,*], Kun Yuan [c], Ren Wang [a,b], Xiaofeng Xu [a,b], Xiaoming Zhang [a,b], Luheng Bai [a,b], Qian Feng [a,b], Kurt O. Konhauser [d]

[a] Key Laboratory of Tectonics and Petroleum Resources of Ministry of Education, China University of Geosciences, Wuhan, 430074, China
[b] School of Earth Resources, China University of Geosciences, Wuhan, 430074, China
[c] Oil and Gas Survey Center, China Geological Survey, Beijing, 100029, China
[d] Department of Earth and Atmospheric Sciences, University of Alberta, Edmonton, Alberta, T6G 2E3, Canada

ARTICLE INFO

Keywords:
Marine sediment
Organic-rich mudstone
Paleoenvironmental condition
Organic matter accumulation
Middle Devonian Eifelian
Youjiang Basin

ABSTRACT

The Nabiao Formation of the Middle Devonian Eifelian period has been identified as a promising site for shale gas exploration in the Youjiang Basin, South China. And yet, little is known about the accumulation mechanism of organic matter under transgression in the archipelago paleogeography. In this study, the core samples were analyzed by thin section microscopy, field emission-scanning electron microscopy, pyrite morphology, X-ray diffraction, and geochemical analysis (total organic carbon (TOC) content, sulfur content, organic petrography, inorganic carbon isotope and major and trace elements) to understand changes in and controls on the mineralogy, lithofacies, depositional environments, as well as the organic matter accumulation mechanism of the Nabiao Formation. The study indicates that organic-rich sediments were deposited during the two transgressions of the Chotec Event and the Kacak Event. The deposition of carbonaceous mudstone occurred in water columns with weak upwelling, while siliceous mudstone and siliceous shale were developed in a strong upwelling water column. The correlations between multiple geochemical proxies (paleoredox, paleoproductivity, and terrestrial detrital influx) and TOC content indicate that the Chotec Event is more conducive to organic matter enrichment of the Nabiao Formation than the Kacak Event. In stage 1, TOC content is low due to oxic water columns and low productivity. In stage 2, the Chotec Event causes the relative sea-level of Member 2 to rise rapidly and the basin bottom water to quickly change to dysoxic conditions. This is the key to organic matter enrichment. In stage 3, the oceanic upwelling is crucial in organic matter enrichment by increasing paleoproductivity. Under the protection of dysoxic condition, organic matter is accumulated in stage 4. Organic matter of the Nabiao Formation is not significantly affected by the terrigenous detrital flux. By taking into account the changes in paleoproductivity, redox conditions, upwelling events, and terrigenous detrital flux, an evolution model is proposed in this paper to elucidate the paleoenvironmental change and the organic matter enrichment under transgression in the archipelago paleogeography.

1. Introduction

Mudstone development not only records the characteristics of environmental evolution such as ancient oceans, paleobiology, and paleoclimate, but also serves as a carrier of oil and gas resources (Aplin and Macquaker, 2011; Xu et al., 2023). The accumulation of organic matter in marine source rocks is often the result of multiple factors, such as primary productivity, redox, sedimentation rate, terrestrial debris flux, etc. (Algeo et al., 2010; Blattmann et al., 2019; Tang et al., 2020; Wei et al., 2022). Therefore, the mechanism of organic matter enrichment in mudstone has always been a focus of attention. The organic matter concentration in marine mudstone is determined by several factors, including biological productivity, preservation conditions, and sedimentation rates. Based on the relative importance of these factors, preservation and productivity models can be distinguished (Tyson, 1995; Yuan et al., 2020). The first model focuses on the conservation of

* Corresponding author. Key Laboratory of Tectonics and Petroleum Resources of Ministry of Education, China University of Geosciences, Wuhan, 430074, China.
E-mail address: shiwz@cug.edu.cn (W. Shi).

https://doi.org/10.1016/j.geoen.2023.212419
Received 14 June 2023; Received in revised form 23 August 2023; Accepted 18 October 2023
Available online 22 October 2023

organic matter resulting from restricted basins causing anoxic water column conditions. In contrast, the second model prioritizes the development of abundant organic matter through elevated paleoproductivity rates (Ross and Bustin, 2009; Sweere et al., 2016; Wang et al., 2019). In fact, it is the working together of these two models that complicates the process of organic matter enrichment (Hou et al., 2022). Furthermore, environmental factors, i.e., tectonic movement and climatic shift, greatly influence the degree of organic matter enrichment during the sedimentary period (Zou et al., 2018; Hu et al., 2021). Therefore, it is necessary to investigate multiple aspects such as paleogeography and geological events to reconstruct the environmental evolution process during the mudstone sedimentation period and clarify the model of organic matter enrichment.

In the Youjiang Basin, organic-rich mudstone of the Nabiao Formation was widely deposited during the Middle Devonian Eifelian period (Ma et al., 2009b; Yuan et al., 2020). A series of global and regional events, such as climatic perturbations and tectonic movements, have endowed the Givetian sediments with significant heterogeneity characteristics (House, 2002; Qie et al., 2019). The unstable changes in the Chotec Event and the Kacak Event have significant impacts on global sea-level cycles and have been widely recorded in the Nabiao Formation of the Youjiang Basin (Walliser, 1996; Lu et al., 2016). The black organic-rich sediments of the Nabiao Formation were deposited in the basin during the transgression. The intensity and duration of transgression, as well as the paleogeographic pattern, affected the redox, paleoproductivity and terrestrial debris flux in different depositional positions, controlling the distribution of organic-rich mudstone and shale in the Youjiang Basin.

Due to the low exploration level of Devonian mudstone in southern China, little is known about the enrichment mechanism of organic matter in the Nabiao Formation of the Youjiang Basin (Cheng, 2011; Yang et al., 2020). Yuan et al. (2020) attributed organic matter enrichment of the Nabiao Formation to the deep-water basin, where the anoxic bottom water column is the key to the development of organic-rich mudstone. Qie et al. (2019) argued that strong tectonic activity deepened the basin, leading to the preservation of organic matter in an anoxic environment and eventually the deposition of organic-rich mudstone. However, these studies are insufficient to explain the internal relationship between transgression and organic-rich mudstone. In fact, in the archipelago paleogeography, there is even less related exploration. This poses a considerable constraint on the study of mudstone organic matter enrichment mechanism in the archipelago paleogeography, such as the Middle Devonian Xiangzhong Depression, the Late Permian northeastern Sichuan Basin (Lin et al., 2018; Liu et al., 2021), the Late Ordovician Tarim Basin (Xiao et al., 2021), the Appalachian Basin of North America, and the Upper Devonian Western Canada Basin (Chabalala et al., 2020; Mansour et al., 2022). Therefore, it is of great importance to identify the appropriate organic matter accumulation model for this specific sedimentary environment.

To clarify the organic matter accumulation mechanism in the basin, in this study a total of 30 samples from Well ND were chosen. The samples were analyzed by thin section microscopy and field emission-scanning electron microscopy, along with X-ray diffraction and geochemical analysis (TOC content, sulfur content, organic petrography, inorganic carbon isotope and major and trace elements) to identify and quantify the changes in redox condition, paleoproductivity, detrital influx, and mineral compositions. The specific objectives of the study are as follows: (1) to identify the changes in the distribution of organic-rich mudstone and organic-poor mudstone; (2) to explain why organic-rich mudstone can be widely deposited; (3) to clarify the organic matter accumulation processes in mudstone; and (4) to propose a model for the organic matter accumulation in a transgression setting. The findings of this study will serve as a guide for analyzing the spatial and temporal changes of hydrocarbon source rocks in basins characterized by an archipelagic marine environment, such as the Youjiang Basin.

2. Geological setting

The Youjiang Basin, located at the junctions of Southeast Yunnan, Western Guangxi, and Southern Guizhou, is part of the South China Plate (Fig. 1a) (Wang and Groves, 2018). During the Middle Devonian, the Youjiang Basin was located in a transition zone between the Pacific tectonic domain and the Tethys tectonic domain (Fig. 1b) (Qie et al., 2019; Zhang et al., 2019). The Guangxi Movement at the end of the Early Paleozoic led to the development of fractures in the basin. The Yadu-Ziyun-Luodian Fault (F1) is the boundary in the North, and the Funing-Napo Fault (F2) is the boundary in the South (Fig. 1c) (Yu et al., 2018). During the Eifelian period, the Youjiang Basin was located at low latitudes with a climate ranging from tropical to sub-tropical (Fig. 1b) (Zeng et al., 1995; Chen et al., 2001).

Since the Early Devonian, with the south-to-north transgression and the activities along the NE (F1, F2) and NW (F3) trending synsedimentary faults, the archipelago marine paleogeography has emerged (Huang et al., 2020; Shao et al., 2020). During the Eifelian period (387.7 Ma–382.7 Ma), the transgression (the Chotec Event of the early Eifelian and the Kacak Event of the late Eifelian) (Fig. 1d) expanded the sedimentary range of the basin facies (Fig. 1c) (Ma et al., 2009a; Mei et al., 2013; Yang et al., 2023). The organic-rich Nabiao Formation is mainly composed of siliceous shale, mudstone, and carbonaceous mudstone with siliceous nodules. Well ND was located in the deep-water rift trough (the Nandan Rift Trough) during the Eifelian period. The mudstone was developed as a whole in the Nabiao Formation (Fig. 1d). The siliceous shale and siliceous mudstone were developed in the middle part and the thin layers of argillaceous limestone and calcareous mudstone were deposited at the bottom (Fig. 1d).

3. Methodology

3.1. Samples

A total of 30 core samples were collected for X-ray diffraction (XRD), thin section optical microscopy and Field Emission-Scanning Electron Microscopy (FE-SEM) to reflect the petrologic and mineral characteristics of the Nabiao Formation. All samples were further analyzed for TOC content, sulfur content, inorganic carbon isotope ($\delta^{13}C_{PDB}$), organic petrography and major and trace elements (Fig. 1d). It is worth noting that all core samples are fresh before analysis to ensure that the test results accurately reflect the characteristics of sedimentary environments in the Nabiao Formation.

3.2. Analytical methods

For TOC and sulfur content, 30 samples were analyzed by Leco CS-230 Carbon and Sulfur Analyzer at Yangtze University. First of all, all samples were ground to less than 200 mesh. Subsequently, the powdered samples were completely soaked with a solution of hydrochloric acid (HCl) and water with a ratio of 1:7 for a long enough time to effectively remove any trace of carbonate minerals. Next, the surface of all samples was washed three times with distilled water. This is a vital step to meticulously eliminate any residual HCl and maintain the purity of the samples. The dried samples were then put in a combustion-calibrated oven, and the amount of CO_2 generated from the combustion process was calculated as the content of TOC and sulfur. The XRD results of 30 samples are from a Smart Lab SE. Each step of the test for mineral composition strictly follows the Chinese Industry-Standard SY/T 5163-2018.

In order to study the petrographic features of the organic matter in the Nabiao Formation, 30 polished sections were observed under reflected light using NIKON-LV100 microscope with an oil immersion objective at a magnification of 500 times. For all the samples of the Nabiao Formation, the classification of the maceral compositions was carried out according to ICCP's guidelines for sapropelinite (ICCP,

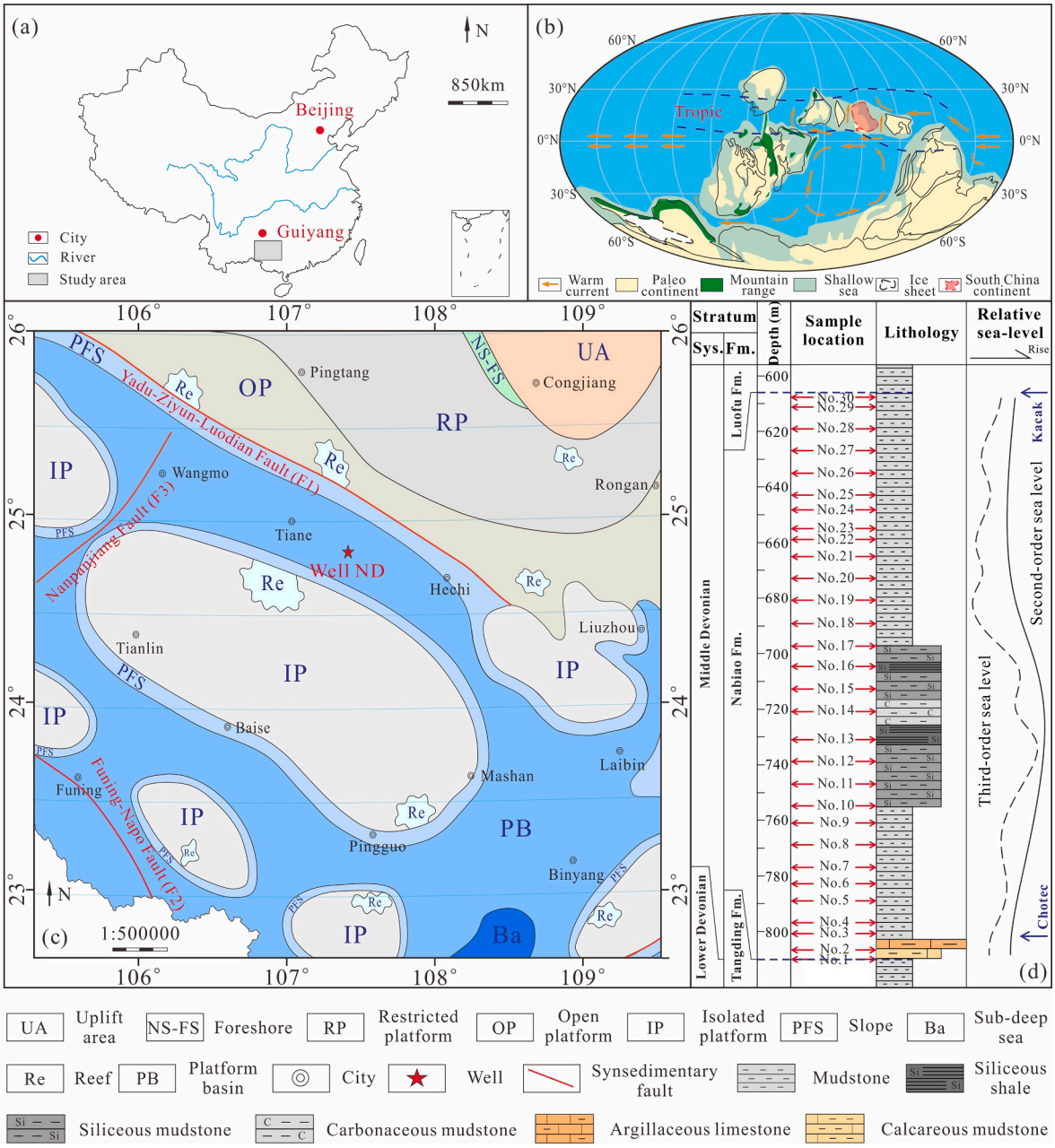

Fig. 1. (a) Location of the study area in China (modified from Yang et al., 2020); (b) Global paleogeography and paleoclimatic reconstructions of the Middle Devonian (Global paleogeography from Scotese and McKerrow, 1990; Zhang et al., 2019; Golonka, 2002. Paleoclimatic reconstructions from Zhang et al., 2019. Ocean current from Scotese, 2001); (c) Palaeogeographic map showing the distribution of sedimentary facies and the location of Well ND (modified from Ma et al., 2009a; Mei et al., 2013); (d) Lithology, sample location and relative sea-level changes (Qie et al., 2019) of Well ND in the Youjiang Basin.

1998), exinite (ICCP, 1998), vitrinite (Taylor and Mclennan, 1985), and inertinite (ICCP, 2001). For the identification of samples, the DM4500P polarized fluorescence microscope was used to analyze kerogen macerals through transmission-fluorescence techniques. For the observation of pyrite framboids and organic matter, the Hitachi S-8000 was used for FE-SEM imaging. More than 100 random pyrite framboids were selected from each section, and their diameters were measured.

GasBench II carbonate device and MAT253 online test were used for the inorganic carbon isotope test. A sample of 50 μg was placed into a 12 ml reaction flask, which was then sealed with an insulating pad to prevent any interference from external factors. Next, the emptying needle was moved in sequence to thoroughly rinse the reaction flask, effectively eliminating any potential influence of air trapped in the flask on the test results. Subsequently, 0.14 ml of 99% phosphoric acid was added into the reaction flask using a precisely calibrated acid needle and acid pump. The reaction between the phosphoric acid and the samples generated carbon dioxide, which was driven by helium to remove any residual water. Finally, the purified carbon dioxide was separated from other impure gases in a chromatographic column maintained at a precisely controlled temperature of 72 °C. The separated carbon dioxide was then introduced into a mass spectrometer to obtain the accurate carbon isotope values. To ensure the reliability of the test results, international standard materials, such as NBS18, NBS19, and LSVEC, were used to calibrate the experimental equipment. Each sample was meticulously analyzed three times to ensure the highest level of accuracy (better than 0.1‰).

For analysis of major and trace element for 30 samples, firstly, the mesh samples were initially baked in an oven at about 110 °C for 13 h to

ensure complete removal of any residual moisture. Approximately 1.2 g of fresh samples were then accurately weighed and subsequently burnt at 1000 °C. After a 2-h heating period, the samples were retrieved and allowed to cool to room temperature. The ignition loss was calculated based on the difference in weight before and after heating. Next, the mixture of samples, cosolvent and oxidant was heated to a molten state for 15 min. The precise heating process was carried out to ensure thorough homogenization of the mixture. The molten mixture was cooled down and solidified to prepare for X-ray fluorescence testing. About 50 mg of fresh samples were acidified to remove organic matter, and then the acidified samples were heated for one day. The samples underwent a continuous evaporation process until drying, followed by repeated treatments of HNO_3 solution. Subsequently, with the addition of a mixed solution of HNO_3, MQ, and an internal standard, the samples were heated for half a day. Finally, the samples were diluted with HNO_3 to prepare for Inductively Coupled Plasma Mass Spectrometry analysis. Replicate analysis of samples and standard samples was made to calibrate the final results.

3.3. Data presentation

Titanium is commonly utilized as an indicator for the presence of clay minerals in fine-grained sediments due to its resistance to weathering and changing that may occur after the sediment deposition (Calvert and Pedersen, 2007). Trace elements consist of both authigenic and terrestrial components, and only authigenic components can providing insights into the paleosedimentary environment (Tribovillard et al., 2006). To eliminate the contribution of terrestrial detritus to elements, other elements are normalized to the titanium content (Xiao et al., 2021). The enrichment factor (X_{EF}) is a parameter that describes the degree of element enrichment, and can also indicate the redox of water columns (Tribovillard et al., 2006). The value of X_{EF} is calculated by the following formula:

$$X_{EF} = (X/Ti)_{sample}/(X/Ti)_{PAAS} \quad (1)$$

where X_{EF} is the enrichment factor of element X, $(X/Ti)_{sample}$ is the ratio of element X to Ti measured in the sample, and $(X/Ti)_{PAAS}$ is the ratio of element X to Ti in the Post-Archean Australian Shale (PAAS) whose value is taken from Taylor and Mclennan (1985). The value of X_{EF} greater than 1.0 indicates an elevated level of element enrichment compared to the standard ratio (Tribovillard et al., 2012; Wang et al., 2019).

The degree of pyritization (DOP) is the ratio of iron in pyrite to total active iron (iron in pyrite and iron dissolved in hydrochloric acid) (Raiswell et al., 1988). The iron content in pyrite is similar to that of minerals, so DOP_T can take the place of DOP, as astutely noted by Raiswell and Berner (1986). In estimating iron content in pyrite, it is assumed that sulfur is in the form of FeS_2 (Rimmer, 2004; Rowe et al., 2008). The value of DOP_T is calculated by the following formula:

$$DOP_T = (55.85/64.16) \times S/Fe \quad (2)$$

where 64.16 and 55.85 are the atomic masses of S and Fe. S is the measured inorganic sulfur content and Fe is the content of total iron in a sample.

To quantify the paleoproductivity levels, the concentration of biogenic silica (Si_{bio}) or biogenic barium (Ba_{bio}) is determined by subtracting the detrital silicon (Si) or barium (Ba) fraction from the total silicon or barium concentration according to the following equations, respectively (Schoepfer et al., 2015):

$$Si_{bio} = [Si_{sample}] - [Ti_{sample} \times (Si/Ti)_{PAAS}] \quad (3)$$

$$Ba_{bio} = [Ba_{sample}] - [Ti_{sample} \times (Ba/Ti)_{PAAS}] \quad (4)$$

where Si_{sample}, Ti_{sample}, and Ba_{sample} are the measured contents of silicon (Si), titanium (Ti), and barium (Ba) in the mudstone samples, respectively. These values represent the actual concentrations of these elements in the samples under investigation. The values of 49.34 and 0.1094 are adopted as the Si/Ti and Ba/Ti ratios, respectively (Taylor and Mclennan, 1985).

The classification of organic matter based on the relative content of microscopic fractions in kerogen can be determined by the value of TI (Zhong et al., 2004) which is calculated by the following formula:

$$TI = \frac{a*(+100) + b*(+50) + c*(-75) + d*(-100)}{100} \quad (5)$$

where a, b, c, and d are the relative contents of sapropelinite, exinite, vitrinite, and inertinite in the sample, respectively. The kerogen of type I: $80 < TI < 100$, the kerogen of type II_1: $40 < TI < 80$, the kerogen of type II_2: $0 < TI < 40$, and the kerogen of type III: $TI < 0$.

4. Results

4.1. Sequence stratigraphy

A sequence stratigraphic framework requires: (1) evidence of chronostratigraphic equivalency of adjacent datasets using geological age or seismic data; and (2) data across the basin to observe the basin-scale trends. Numerous previous studies have consistently shown a correlation between higher GR values and the increasing clay content in mudstone as water columns deepen during the deposition phase (Singh, 2008). In general, it has been accepted that such trends can be interpreted as T-R (transgressive/regressive) cycles related to system tracts (Abouelresh and Slatt, 2012). Therefore, the lithology (lithofacies and mineral content) and GR values can be used as sensitive indicators for identifying sequence boundaries (Luning et al., 2000). Based on the previous sequence stratigraphic framework (Abouelresh and Slatt, 2012; Gradstein, 2020), the stratigraphic sequences of the Nabiao Formation in Well ND are determined according to the above indicators (Fig. 2).

Sequence Boundary #1 (SB1): SB1 was identified due to the lithological differences between the Tangding Formation and the Nabiao Formation (Fig. 2). Mudstone and calcareous mudstone are located below and above SB1, respectively. Sequence Boundary #2 (SB2): SB2 was identified due to the lithological differences and GR curve changes (Fig. 2). Mudstone (the higher GR values) is deposited above SB2 interface, while argillaceous limestone (the lower GR values) is below it. Sequence Boundary #3 (SB3): SB3 was identified due to the differences in lithology and lithofacies (Fig. 2). Above SB3 interface, siliceous mudstone of S-3 dominates, while below the interface, mudstone of CM-1 is mainly present. Sequence Boundary #4 (SB4): SB4 was identified based on the notable changes in lithology and lithofacies (Fig. 2). Above SB4 interface, mudstone of M-2 is predominantly present, while below the interface, siliceous mudstone S-3 dominates. Sequence Boundary #5 (SB5): SB5 was identified due to the lithological differences between the Nabiao Formation and the Luofu Formation (Fig. 2).

Based on the identification of SBs, four third-order sequences of the Nabiao Formation were interpreted. Each sequence was composed of a lower transgressive system tract (TST) and an upper regressive system tract (RST) (Fig. 2). The boundary between a TST and RST was identified as a maximum flooding surface (mfs) which corresponds to a relatively high GR value and mudstone content (Fig. 2). According to SBs, TSTs and RSTs, the sedimentary environment indicators and organic matter accumulation factors will be discussed in four members (Figs. 2 and 6).

4.2. Mineral components and lithofacies

The XRD mineralogical analysis suggests that the Nabiao Formation comprises silicate minerals and clay minerals (Fig. 3). Distinct differences in mineral composition can be observed among different members (Table 1). Member 1 has a higher content of carbonate minerals, ranging from 24.00 wt% to 26.00 wt%, with an average of 25.00 wt%. The clay

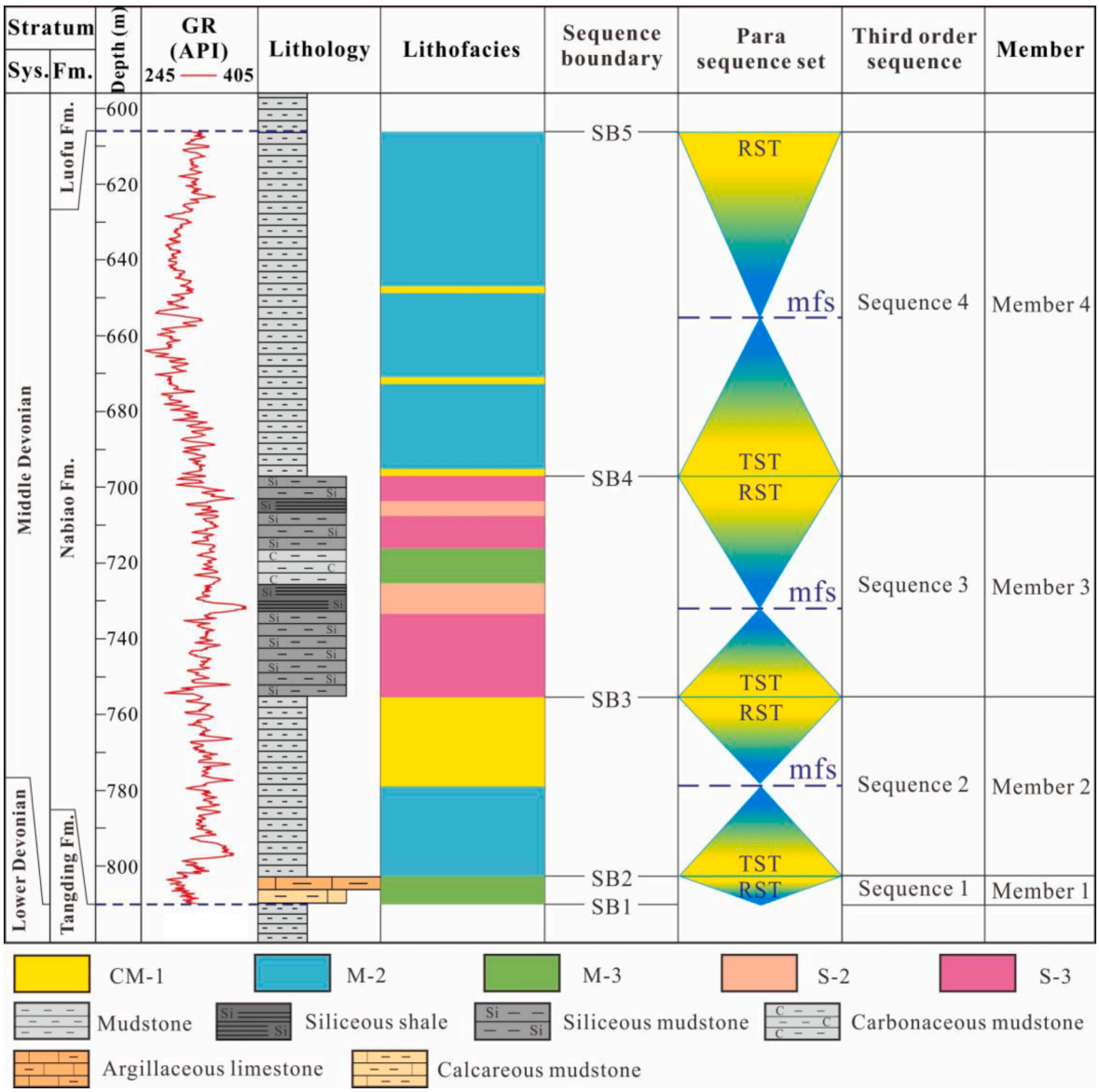

Fig. 2. Lithofacies, GR logging, third-order sequences and members of Well ND. Each lithofacies code (CM-1, etc.) with reference to Fig. 4. The sequence framework of the Nabiao Formation on the basis of previous sequence division results (Gradstein, 2020), characteristics of lithology and lithofacies, and GR curve changes from Well ND.

content slightly exceeds that of the silicate minerals, with clay minerals ranging from 40.00 wt% to 43.00 wt% (average 41.50 wt%), and silicate minerals from 27.00 wt% to 29.00 wt% (average 28.00 wt%). In Member 2, clay minerals are the main mineral components with the content ranging from 41.00 wt% to 52.00 wt% (average 45.14 wt%). In Member 3, silicate minerals are the main mineral components with the content ranging from 31.00 wt% to 70.00 wt% (average 52.00 wt%). In Member 4, the content of silicate minerals (average 38.31 wt%) is slightly lower than that of the clay minerals (average 43.54 wt%). The samples of Members 2 and 4 have relatively higher pyrite content, averaging 4.77 wt% and 3.27 wt%, respectively.

A ternary diagram plotting silicate minerals, carbonate minerals, and clay minerals (Ma et al., 2016; Wu et al., 2016) is shown in Fig. 4. Due to significant differences in mineral compositions, the samples are classified into 3 lithofacies groups and 5 lithofacies, including S-2, S-3, M-2, M-3, and CM-1 (Fig. 2). The calcareous mudstone is almost mixed lithofacies shale (M-3) in Member 1. In Member 2, the upper mudstone, with high clay mineral content, belongs to silica-rich argillaceous shale lithofacies (CM-1), and the lower part of mudstone belongs to argillaceous/siliceous mixed shale lithofacies (M-2). In Member 3, the siliceous shale is mixed siliceous lithofacies shale (S-2), and the siliceous mudstone belongs to clay-rich siliceous lithofacies shale (S-3). In Member 4, the mudstone is mainly argillaceous/siliceous mixed lithofacies shale (M-2), with few being silica-rich argillaceous lithofacies (CM-1).

4.3. Petrological characteristics

Along with the appearance of limestone laminae (Fig. 5a), a large number of broken shells (Fig. 5b) are found in calcareous mudstone of Member 1. There is a clear lithological boundary between argillaceous limestone in the upper part of Member 1 and mudstone at the bottom of Member 2 (Fig. 5c). It can be seen that there are a small number of silicate minerals with small diameter in mudstone of Member 2 (Fig. 5d). In Member 3, the content of silicate minerals significantly increases. Spotted silicate minerals are surrounded by a large amount of mudstone in siliceous mudstone (Fig. 5e). Silicon is enriched in siliceous shale in bands (Fig. 5f) and clumps (Fig. 5g). Mudstone has a relatively high TOC

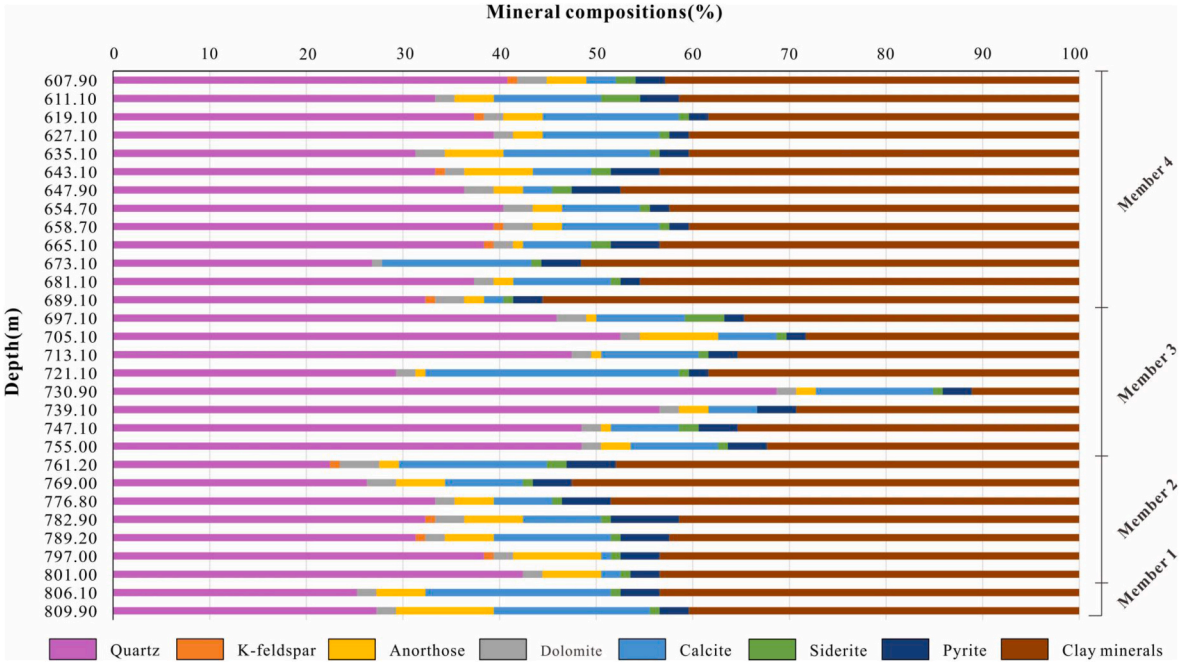

Fig. 3. The mineral composition and content results of each sample in the Nabiao Formation.

Table 1
Mineral and TOC content of each sample in the Nabiao Formation.

Sample No.	Depth/m	Member	Clay/%	Quartz%	K-feldspar%	Anorthosite%	Calcite%	Dolomite%	Siderite%	Pyrite%	TOC/%	S/%
No.1	809.90	1	40.00	27.00	0.00	2.00	10.00	16.00	2.00	3.00	1.20	0.41
No.2	806.10	1	43.00	25.00	0.00	2.00	5.00	19.00	2.00	4.00	1.31	0.77
No.3	801.00	2	43.00	42.00	0.00	2.00	6.00	2.00	2.00	3.00	2.63	1.42
No.4	797.00	2	43.00	38.00	1.00	2.00	9.00	1.00	2.00	4.00	2.72	1.67
No.5	789.20	2	42.00	31.00	1.00	2.00	5.00	12.00	2.00	5.00	2.75	1.69
No.6	782.90	2	41.00	32.00	1.00	3.00	6.00	8.00	2.00	7.00	2.31	2.34
No.7	776.80	2	48.00	33.00	0.00	2.00	4.00	6.00	2.00	5.00	2.12	1.83
No.8	769.00	2	52.00	26.00	0.00	3.00	5.00	8.00	2.00	4.00	2.43	2.57
No.9	761.20	2	47.00	22.00	1.00	4.00	2.00	15.00	4.00	5.00	2.46	1.83
No.10	755.00	3	32.00	48.00	0.00	2.00	3.00	9.00	2.00	4.00	2.12	1.75
No.11	747.10	3	35.00	48.00	0.00	2.00	1.00	7.00	3.00	4.00	2.67	1.97
No.12	739.10	3	29.00	56.00	0.00	2.00	3.00	5.00	1.00	4.00	3.05	2.19
No.13	730.90	3	11.00	68.00	0.00	2.00	2.00	12.00	2.00	3.00	3.86	3.21
No.14	721.10	3	38.00	29.00	0.00	2.00	1.00	26.00	2.00	2.00	2.88	2.16
No.15	713.10	3	35.00	47.00	0.00	2.00	1.00	10.00	2.00	3.00	3.33	1.90
No.16	705.10	3	23.00	58.00	0.00	2.00	8.00	6.00	2.00	2.00	3.05	1.79
No.17	697.10	3	34.00	45.00	0.00	3.00	1.00	9.00	4.00	4.00	2.83	2.68
No.18	689.10	4	55.00	32.00	1.00	3.00	2.00	2.00	2.00	3.00	2.78	1.99
No.19	681.10	4	45.00	37.00	0.00	2.00	2.00	10.00	2.00	2.00	2.33	1.11
No.20	673.10	4	50.00	26.00	0.00	1.00	0.00	15.00	4.00	4.00	2.19	1.29
No.21	665.10	4	43.00	38.00	1.00	2.00	1.00	7.00	3.00	5.00	2.59	1.66
No.22	658.70	4	40.00	39.00	1.00	3.00	3.00	10.00	2.00	2.00	2.18	1.38
No.23	654.70	4	42.00	40.00	0.00	3.00	3.00	8.00	2.00	2.00	2.55	1.07
No.24	647.90	4	47.00	36.00	0.00	3.00	3.00	3.00	3.00	5.00	2.34	1.03
No.25	643.10	4	43.00	33.00	1.00	2.00	7.00	6.00	3.00	5.00	2.41	1.42
No.26	635.10	4	40.00	31.00	0.00	3.00	6.00	15.00	2.00	3.00	1.92	1.19
No.27	627.10	4	40.00	39.00	0.00	2.00	3.00	12.00	2.00	2.00	1.37	1.34
No.28	619.10	4	38.00	37.00	1.00	2.00	4.00	14.00	2.00	2.00	2.08	1.56
No.29	611.10	4	41.00	33.00	0.00	2.00	4.00	11.00	5.00	4.00	2.42	1.79
No.30	607.90	4	42.00	40.00	1.00	3.00	4.00	3.00	4.00	3.00	2.90	1.91

content in Member 3. As shown in Fig. 5h, a lot of organic matter is developed. Compared with Member 3, mudstone content of Member 4 decreases and carbonate mineral content increases (Fig. 5i).

4.4. TOC content and organic matter petrography

There is a significant change in TOC content of the samples from different members (Fig. 6; Table 1). Member 1 has relatively low TOC content (average 1.26%). TOC content of 7 samples from Member 2 ranges between 2.12% and 2.75% (average 2.49%). TOC content of 8 samples from Member 3 ranges between 2.12% and 3.86% (average 2.97%), showing relatively high TOC content in the Nabiao Formation. In Member 4, TOC content of 13 samples ranges between 1.37% and 2.90% (average 2.31%). TOC content of the Nabiao Formation shows a trend of first increasing and then decreasing from Member 1 to Member 4 (Fig. 6).

Polished sections suggest that organic matter of the Nabiao Formation is composed of sapropelinite (Figs. 7a, b, and g), exinite (Fig. 7c),

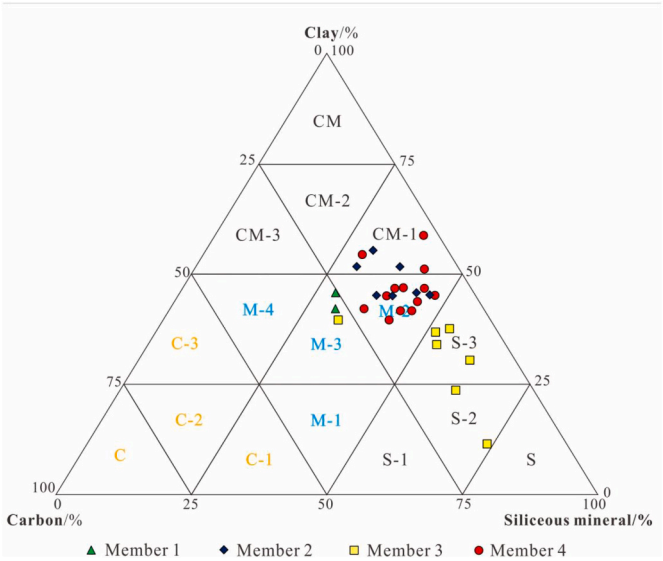

Fig. 4. Ternary diagram (modified from Ma et al., 2016; Wu et al., 2016) shows the mineralogical composition of five lithofacies in Well ND. S-2: Mixed siliceous shale lithofacies; S-3: Clay-rich siliceous shale lithofacies; M-2: Argillaceous/siliceous mixed shale lithofacies; M-3: Mixed shale lithofacies; CM-1: Silica-rich argillaceous shale lithofacies.

vitrinite (Figs. 7d–e, and h–k) and inertinite (Figs. 7f, and l). Sapropelinite is a component formed by algae after sapropelic action (ICCP, 1998). At the overmature stage, residual algal forms are visible, with no fluorescence display (Figs. 7a and b). Exinite is generally the reproductive organ of higher plants (ICCP, 1998). It appears grayish white under white reflected light in the Nabiao Formation (Fig. 7c). Vitrinite is derived from botanical tissues, such as roots, barks, and leaves. And lignin and/or carbohydrates are the main components of botanical tissues (ICCP, 1998). Under oil-immersed reflected light, over-mature vitrinite appears gray with high relief (Fig. 7d and e). Inertinite is usually ascribed to the source of fire-derived charcoal, aerobic activity of microorganism and fungus, and biochemical alteration (ICCP, 1998; ICCP, 2001). Inertinite particles are brighter, fragmented and plate-like (Fig. 7f).

A large amount of sapropelinite presenting amorphous algae can be seen in Member 3 (Fig. 7g). The values of TI show that the whole kerogen belongs to Type I (Appendix 1). In Member 2, the amount of sapropelinite decreases, and that of vitrinite increases (Fig. 7h), and as a result, the kerogen of Type II_1 is developed (Appendix 1). In Member 4, a large amount of vitrinite is developed (Fig. 7i), and the kerogen almost belongs to type II_1 (Appendix 1). In Member 1, a large amount of vitrinite (Figs. 7j, and k) and a small amount of inertinite (Fig. 7l) are developed, and as a result, the kerogen belongs to Type II_2 (Appendix 1).

4.5. Petrographic features of pyrite

Based on observations made using SEM and polished sections, it is evident that pyritic framboids are significantly abundant in Member 2, Member 3, and Member 4, but almost absent in Member 1 (Figs. 8a–h). There are various pyrite morphologies in the Nabiao Formation, including normal framboids (Figs. 8c–f), euhedral pyrites (Figs. 8a–b, and g–h), and clustered pyrites (Fig. 8h). In Member 1, a lot of euhedral pyrites can be seen with significant diameter differences. Euhedral pyrites and organo-mineral complexes coexist in calcareous mudstone (Figs. 8a and b). Except 1 group, the normal framboids (Figs. 8j and k) are the main pyrite type (Figs. 8c–g). In Member 2, the diameter of pyrite framboid is mainly 5.00–7.00 μm (mean 5.20–6.88 μm) (Figs. 9a–c). In Member 3, the framboidal pyrites are abundant, almost 3.00–5.00 μm (mean 3.55–4.25 μm) (Figs. 9d–f). In Member 4, a few clustered pyrites can be seen (Fig. 8h), and the framboidal pyrites are almost at the bottom, generally 8.00–10.00 μm (mean 8.85–9.55 μm) (Figs. 9g–i).

4.6. Inorganic carbon isotope

Only when Mn/Sr value is less than 10, can the $\delta^{13}C_{PDB}$ record the carbonate primary carbon isotopic signature (Heath et al., 2021; Hu et al., 2021; Lan, 2022). Therefore, the values of Mn/Sr in the samples of the Nabiao Formation were calculated, before using the $\delta^{13}C_{PDB}$ values of Well ND. Mn/Sr values range from 0.71 to 2.27, with an average of 1.19, all of which are less than 3 (Table 2), indicating that the $\delta^{13}C_{PDB}$ values of all samples are representative of the initial values of the original seawater.

For samples of the Nabiao Formation, the $\delta^{13}C_{PDB}$ values of Member 3 are generally high, while the low $\delta^{13}C_{PDB}$ values are in Member 1 and the upper of Member 4. The $\delta^{13}C_{PDB}$ values show a trend of initially ascending and subsequently descending from the lower Nabiao Formation to the upper member (Fig. 6).

4.7. Elemental geochemistry

4.7.1. Major elements

The main major elements, expressed as oxides, are listed in Table 2. The SiO_2 content initially shows an upward trend until Member 3, followed by a subsequent downward trend, which is consistent with the trend revealed by the XRD results (Table 1). In Member 1, the contents of SiO_2 (average 23.16 wt%) and Si_{bio} (average 0.00 %) are significantly lower than those of other members. In Member 2, the content of SiO_2 ranges from 21.36 wt% to 46.73 wt% (average 35.89 wt%), and that of Si_{bio} from 2.51 wt% to 11.45 wt% (average 7.39 wt%). In Member 3, the SiO_2 content is relatively high (average 45.51 wt%), accompanied by the appearance of relatively high concentration of Si_{bio} (average 10.26 wt %). In Member 4, the content of SiO_2 ranges from 21.53 wt% to 45.94 wt % (average 34.66 wt%), and that of Si_{bio} from 0.00 wt% to 9.49 wt% (average 4.86 wt%). The relative concentrations of Al_2O_3, CaO, Fe_2O_3 and TiO_2 exhibit inconspicuous vertical fluctuation in the Nabiao Formation. There is relatively high content of Al_2O_3 (average 9.74 wt%) in Member 2. CaO (average 27.08 wt%), Fe_2O_3 (average 6.06 wt%) and TiO_2 (average 0.39 wt%) are generally enriched in Member 1.

4.7.2. Trace elements

Compared to the average trace element content of the Nabiao Formation mudstone, the content of V, Zn, Mo and Cd shows a depletion in Member 1 and an enrichment in Member 3 (Table 3). Member 1 has average content of V (average 21.26 ppm), Zn (average 104.69 ppm), Mo (average 0.42 ppm) and Cd (average 0.04 ppm), while Member 3 has average contents of V (average 411.30 ppm), Zn (average 230.16 ppm), Mo (average 33.92 ppm) and Cd (average 7.51 ppm), respectively. The relative concentrations of Ba_{bio} and Zn/Ti exhibit noticeable vertical fluctuation in the Nabiao Formation. The values of Ba_{bio} and Zn/Ti show a trend of first increasing and then decreasing from Member1 to Member 4. Member 3 has relatively high values of Ba_{bio} (average 920.87%) and Zn/Ti (average 1095.72). In addition, the samples of Member 3 have higher values of Cd/Mo (average 0.23) and lower values of Co × Mn (average 0.27 ppm/%).

5. Discussion

5.1. Terrestrial detrital influx

The enrichment of organic matter is influenced by various factors. One of them is the influx of terrestrial detritus which can directly impact the enrichment of organic matter by diluting its concentration (Algeo and Maynard, 2004; Wu et al., 2020; Hou et al., 2022), or act as a sorbent to facilitate organic matter accumulation (Wang et al., 2019) and

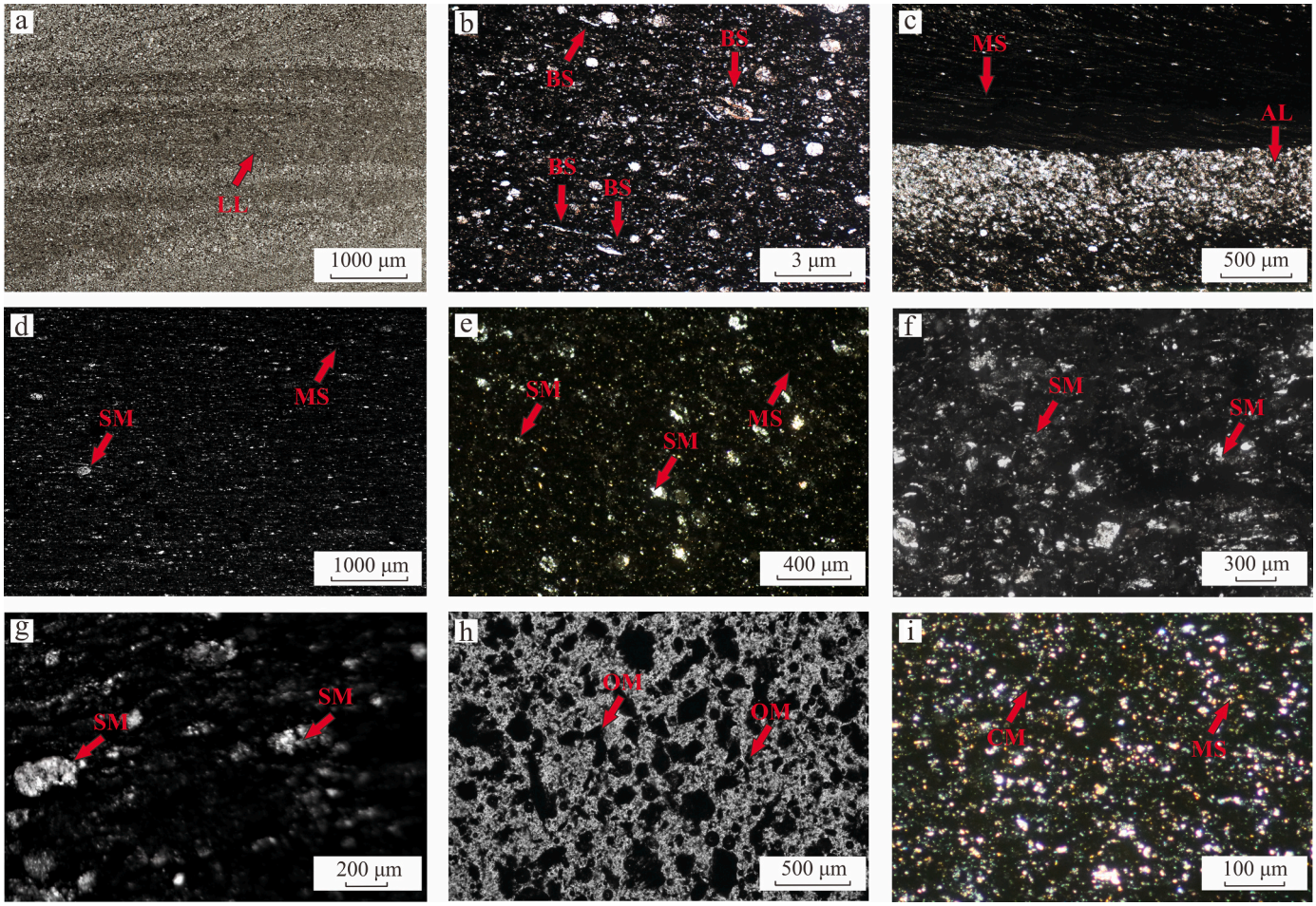

Fig. 5. Thin section optical microscopy images of representative minerals and rocks in the Nabiao Formation. (a) The limestone laminae of calcareous mudstone (809.90 m); (b) A large number of broken shells in calcareous mudstone (808.60 m); (c) The lithological boundary between mudstone and argillaceous limestone (802.85 m); (d) A small number of silicate minerals in mudstone (759.00 m); (e) A small number of silicate minerals in siliceous mudstone (739.00 m); (f) A large number of siliceous materials in siliceous shale (731.00 m); (g) A large number of siliceous materials in siliceous shale (705.00 m); (h) A large amount of organic matter in carbonaceous mudstone (721.00 m); (i) The carbonate minerals in mudstone (627.00 m); LL = limestone laminae; BS = broken shell; MS = mudstone; AL = argillaceous limestone; SM = silicate mineral; OM = organic matter; CM = carbonate mineral.

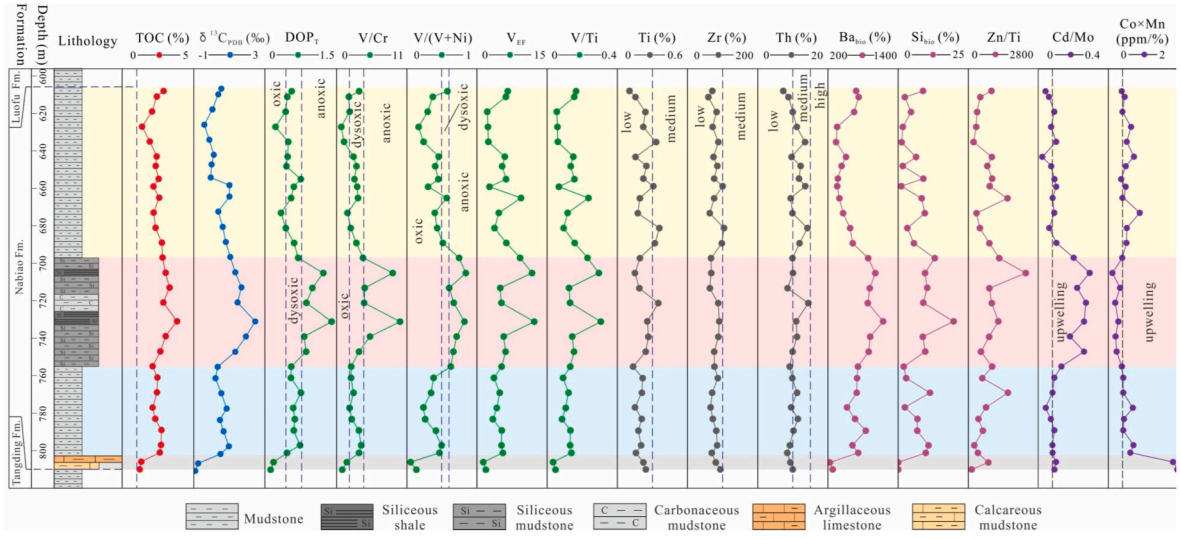

Fig. 6. Vertical variations of various geochemical indexes in the Nabiao Formation of Well ND. Representative concentrations of Ba and Si from PAAS vs. Ti (Ba/Ti = 0.0065; Si/Ti = 2.93) and the indicative meanings of all analysis indexes are represented by black vertical dashed lines (threshold values in Section 5).

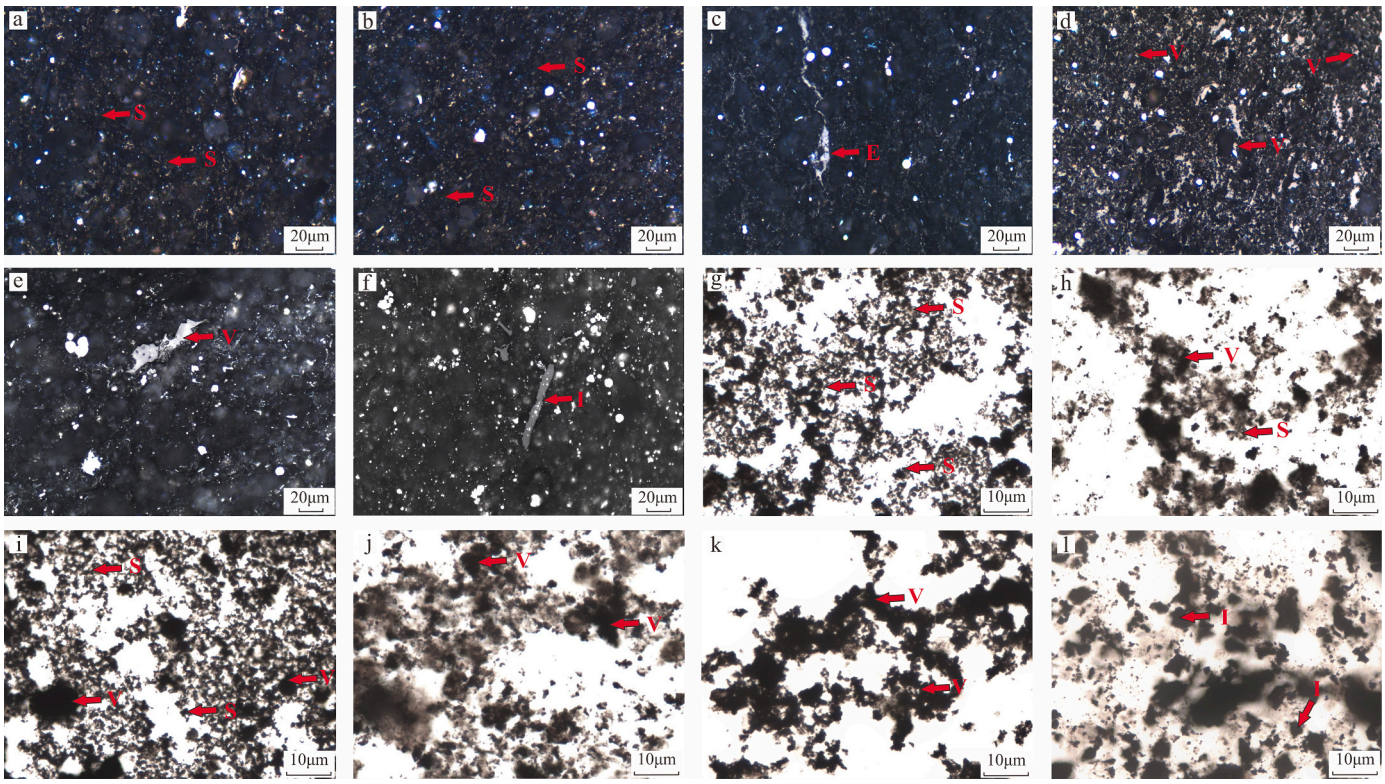

Fig. 7. Photomicrographs of transmission-fluorescence kerogen macerals and organic matter under oil-immersed reflected light. (a) Sapropelinite (721.00 m); (b) Sapropelinite (731.00 m); (c) Exinite (776.80 m); (d) Vitrinite (647.90 m); (e) Vitrinite (806.10 m); (f) Inertinite (809.90 m); (g) A large amount of sapropelinite (721.00 m); (h) A small amount of sapropelinite and a large amount of vitrinite (776.80 m); (i) A small amount of sapropelinite and a large amount of vitrinite (647.90 m); (j) A large amount of vitrinite (806.10 m); (k) A large amount of vitrinite (809.90 m); (l) A small amount of inertinite (809.90 m); S = sapropelinite; E = exinite; V = vitrinite; I = inertinite.

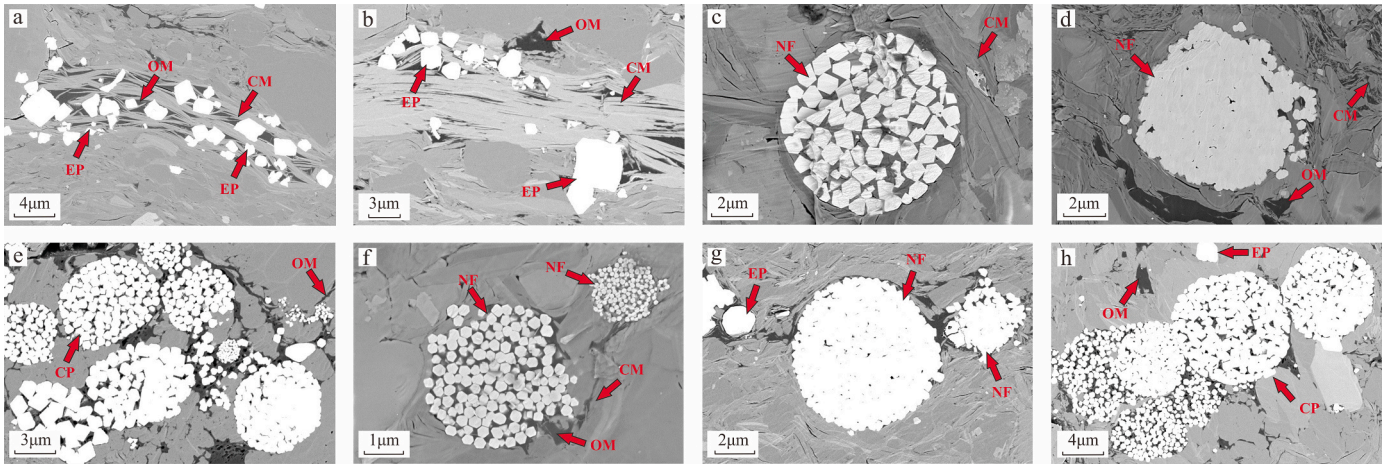

Fig. 8. SEM photos of pyrite in the Nabiao Formation. (a) Coexistence of euhedral pyrites and organo-mineral complexes (809.90 m); (b) Euhedral pyrites with significant diameter differences (808.60 m); (c) A small number of normal framboids (789.20 m); (d) Coexistence of normal framboids and organic matter (761.20 m); (e) A large number of normal framboids (730.90 m); (f) Coexistence of a lot of organic matter and normal framboids (721.10 m); (g) A scant presence of organic matter and normal framboids with significant diameter differences (689.10 m); (h) Euhedral pyrites and clustered pyrites with significant diameter differences (627.10 m); OM= organic matter; CM= clay mineral; NF= normal framboid; EP= euhedral pyrite; CP= clustered pyrite.

rate of settling (Playter et al., 2017).

Terrigenous detritus typically contains quartz, feldspar, and clay minerals, among which the content of elements Ti, Si, Zr, and Al is commonly used as the indicator of the terrestrial detrital influx (Lash and Blood, 2014; Elbra et al., 2023). The correlation between Al and Zr or Th is low (R^2 = 17.17% and 26.18%, respectively) (Figs. 10a and b). In contrast, the correlation diagram demonstrates a significantly positive association between Ti and Zr, with R^2 values of 63.37% and 76.95%, respectively (Figs. 10c and d). The anomalies in the content of element Al may result from the presence of authigenic clay minerals. Therefore, elements Ti, Th, and Zr are more suitable for reflecting the terrestrial detrital influx, and element Ti can be used for elemental normalization.

As illustrated in Fig. 6, in all samples of the Nabiao Formation, there

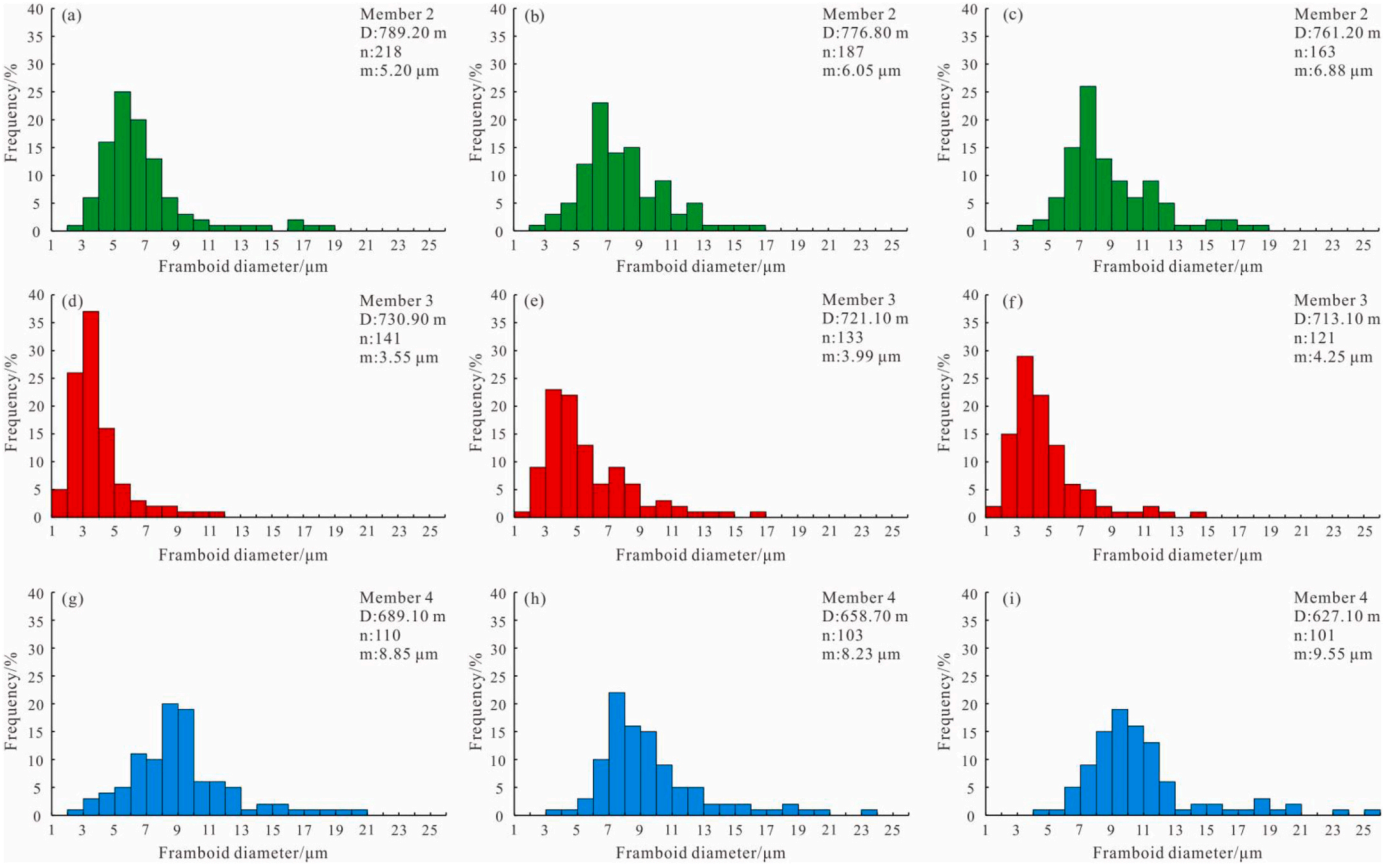

Fig. 9. Histograms of the distribution of pyrite framboid diameter of Member 2 (a–c), Member 3 (d–f) and Member 4 (g–i) in the Nabiao Formation, D = depth, n = quantity of measured framboids, m = average diameter of framboids.

Table 2
Partial major oxide content and corresponding analysis indices of each sample in the Nabiao Formation.

Sample No.	Depth/ m	Member	SiO_2	TiO_2	Al_2O_3	Fe_2O_3	MnO	CaO	K_2O	Si/%	Si_{bio}/ %	Ti/ %	Al/ %	Fe/ %	Mn/ %	DOP_T	$\delta^{13}C_{PDB}$
No.1	809.90	1	24.02	0.41	7.11	5.77	0.03	11.00	2.19	11.21	0.00	0.24	3.76	4.04	0.03	0.09	−0.89
No.2	806.10	1	22.30	0.37	9.39	6.36	0.06	43.15	1.41	10.40	0.00	0.22	4.97	4.45	0.05	0.15	−0.73
No.3	801.00	2	38.10	0.26	10.54	4.03	0.03	11.19	2.89	17.78	9.94	0.16	5.58	2.82	0.03	0.44	0.52
No.4	797.00	2	44.93	0.34	13.88	2.90	0.04	13.76	2.67	20.97	10.94	0.20	7.35	2.03	0.03	0.72	0.98
No.5	789.20	2	33.86	0.30	7.99	3.60	0.03	6.13	3.18	15.80	6.92	0.18	4.23	2.52	0.02	0.58	0.69
No.6	782.90	2	37.00	0.35	9.68	4.80	0.03	6.51	3.02	17.27	7.00	0.21	5.12	3.36	0.02	0.61	0.48
No.7	776.80	2	21.36	0.25	4.61	3.98	0.02	5.02	2.77	9.97	2.51	0.15	2.44	2.79	0.02	0.57	0.86
No.8	769.00	2	46.73	0.35	12.91	4.34	0.03	5.64	2.82	21.81	11.45	0.21	6.83	3.04	0.02	0.74	0.56
No.9	761.20	2	29.27	0.36	8.58	4.35	0.02	6.23	3.15	13.66	2.98	0.22	4.54	3.04	0.02	0.52	0.23
No.10	755.00	3	18.49	0.22	6.27	4.11	0.05	41.61	1.16	8.63	1.99	0.13	3.32	2.88	0.04	0.53	0.36
No.11	747.10	3	46.36	0.40	7.05	2.89	0.02	2.28	3.05	21.64	9.65	0.24	3.73	2.02	0.02	0.85	1.34
No.12	739.10	3	46.89	0.44	6.34	3.38	0.03	4.36	2.63	21.88	8.79	0.27	3.35	2.37	0.02	0.81	1.94
No.13	730.90	3	69.39	0.43	10.96	2.87	0.05	11.90	2.67	32.38	19.75	0.26	5.80	2.01	0.04	1.39	2.46
No.14	721.10	3	56.07	0.58	16.12	3.15	0.02	2.74	3.63	26.17	8.91	0.35	8.53	2.20	0.02	0.85	1.47
No.15	713.10	3	42.03	0.31	4.92	2.41	0.05	50.02	1.92	19.61	10.32	0.19	2.60	1.68	0.04	0.98	1.69
No.16	705.10	3	36.44	0.25	5.75	1.83	0.02	5.68	2.49	17.01	9.60	0.15	3.04	1.28	0.02	1.21	1.34
No.17	697.10	3	48.37	0.32	3.69	4.92	0.06	17.89	1.42	22.57	13.04	0.19	1.95	3.45	0.05	0.68	1.06
No.18	689.10	4	45.94	0.53	8.25	4.19	0.03	4.61	2.91	21.44	5.62	0.32	4.37	2.94	0.02	0.59	0.81
No.19	681.10	4	45.00	0.60	10.60	3.34	0.03	4.45	3.18	21.00	3.28	0.36	5.61	2.34	0.02	0.41	0.64
No.20	673.10	4	38.80	0.29	3.85	5.15	0.08	20.09	1.30	18.11	9.49	0.17	2.04	3.60	0.06	0.31	0.39
No.21	665.10	4	38.58	0.32	5.80	3.92	0.02	9.47	2.35	18.01	8.50	0.19	3.07	2.74	0.02	0.53	1.02
No.22	658.70	4	26.96	0.51	12.06	2.94	0.02	3.24	3.22	12.58	0.00	0.31	6.38	2.06	0.01	0.58	1.02
No.23	654.70	4	42.99	0.37	12.45	1.81	0.02	9.34	2.68	20.06	9.09	0.22	6.59	1.27	0.02	0.73	−0.03
No.24	647.90	4	30.00	0.41	9.14	3.00	0.03	6.73	2.75	14.00	1.74	0.25	4.84	2.10	0.02	0.43	0.02
No.25	643.10	4	30.29	0.26	10.87	3.90	0.03	5.88	3.01	14.14	6.50	0.15	5.75	2.73	0.03	0.45	0.14
No.26	635.10	4	38.02	0.55	10.16	3.18	0.03	7.28	2.69	17.74	1.36	0.33	5.38	2.23	0.02	0.47	−0.11
No.27	627.10	4	27.03	0.37	13.14	8.63	0.08	18.61	1.73	12.61	1.67	0.22	6.96	6.04	0.06	0.19	−0.39
No.28	619.10	4	35.21	0.40	14.39	4.73	0.05	11.36	2.62	16.43	4.58	0.24	7.62	3.31	0.04	0.41	0.06
No.29	611.10	4	21.53	0.26	7.12	5.00	0.09	17.30	1.52	10.05	2.39	0.16	3.77	3.50	0.07	0.45	0.39
No.30	607.90	4	30.24	0.17	5.05	4.41	0.06	4.37	2.70	14.11	8.99	0.10	2.68	3.09	0.04	0.54	0.56

Table 3
Partial trace element content and corresponding analysis indices of each sample in the Nabiao Formation.

Sample No.	No.1	No.2	No.3	No.4	No.5	No.6	No.7	No.8	No.9	No.10	No.11	No.12	No.13	No.14	No.15
Depth/m	809.90	806.10	801.00	797.00	789.20	782.90	776.80	769.00	761.20	755.00	747.10	739.10	730.90	721.10	713.10
Member	1	1	2	2	2	2	2	2	2	3	3	3	3	3	3
V/ppm	31.73	10.78	85.39	103.42	93.58	64.68	61.77	97.75	77.04	177.25	371.56	379.00	783.80	456.90	234.66
Cr/ppm	132.88	47.36	62.76	69.42	68.49	74.93	79.53	96.70	87.48	77.93	106.26	72.58	78.92	106.34	53.38
Ni/ppm	201.50	191.60	96.76	104.16	126.63	183.60	191.56	184.35	125.48	106.06	188.70	155.14	171.43	227.50	154.65
Zn/ppm	32.20	177.18	60.44	48.10	104.40	83.81	106.66	330.82	120.22	127.64	121.94	220.12	305.59	326.84	157.56
Rb/ppm	57.11	32.79	70.57	65.21	84.16	86.95	74.23	78.08	78.64	64.84	83.49	70.60	129.87	88.79	26.43
Sr/ppm	252.52	393.81	249.73	310.69	181.88	185.48	174.98	122.27	180.26	313.55	87.37	131.77	279.60	141.85	394.48
Zr/ppm	93.44	80.54	69.07	84.42	81.83	72.05	65.70	70.08	86.24	76.58	75.91	87.65	90.43	87.37	63.57
Nb/ppm	6.12	6.87	11.96	8.11	8.04	8.50	6.65	9.00	7.84	10.32	11.85	8.26	9.13	10.33	3.93
Ba/ppm	550.21	470.31	901.22	868.10	1065.42	899.04	723.06	924.96	936.99	864.11	1158.89	1214.20	1416.16	1267.11	1123.90
Th/ppm	9.98	9.30	8.41	9.14	10.18	11.43	9.52	11.20	9.85	9.11	9.93	11.19	10.95	14.41	8.51
Mo/ppm	0.33	0.50	14.60	13.20	15.64	17.84	27.67	12.92	34.33	47.20	24.39	28.31	32.95	30.10	41.49
Co/ppm	72.22	39.90	23.13	20.67	20.54	21.25	17.69	19.62	23.12	10.11	13.56	10.32	7.59	10.56	8.98
Cd/ppm	0.03	0.05	1.21	1.06	1.33	1.20	1.11	0.99	3.02	6.32	6.33	5.14	8.69	7.99	9.13
V/Cr	0.88	1.60	3.50	3.84	3.49	2.36	2.02	2.64	2.25	2.27	3.50	5.22	9.93	4.30	4.40
V/(V + Ni)	0.14	0.05	0.47	0.50	0.42	0.26	0.24	0.35	0.38	0.63	0.66	0.71	0.82	0.67	0.60
V_{EF}	0.52	0.19	2.15	2.04	2.08	1.24	1.63	1.86	1.42	5.27	6.12	5.71	12.24	5.23	4.98
V/Ti	0.01	0.00	0.05	0.05	0.05	0.03	0.04	0.05	0.04	0.13	0.15	0.14	0.31	0.13	0.12
Zn/Ti	132.24	796.30	380.46	236.63	579.69	402.65	705.44	1576.26	555.69	948.44	502.03	829.67	1193.31	934.66	836.56
Cd/Mo	0.09	0.10	0.08	0.08	0.09	0.07	0.04	0.08	0.09	0.13	0.26	0.18	0.26	0.27	0.22
Ba_{bio}/%	283.83	226.89	727.42	645.72	868.40	671.33	557.65	695.35	700.31	716.88	893.16	923.95	1136.00	884.55	917.85
Co × Mn/%	1.95	1.83	0.62	0.71	0.42	0.44	0.68	0.42	0.42	0.38	0.23	0.20	0.28	0.19	0.33
Mn/Sr	1.07	1.17	1.07	1.10	1.12	1.10	0.97	1.75	1.01	1.20	1.96	1.50	1.33	1.29	0.93

Sample No.	No.16	No.17	No.18	No.19	No.20	No.21	No.22	No.23	No.24	No.25	No.26	No.27	No.28	No.29	No.30
Depth/m	705.10	697.10	689.10	681.10	673.10	665.10	658.70	654.70	647.90	643.10	635.10	627.10	619.10	611.10	607.90
Member	3	3	4	4	4	4	4	4	4	4	4	4	4	4	4
V/ppm	442.23	445.03	183.41	130.95	79.76	151.23	78.50	133.18	130.94	88.59	71.94	39.83	49.92	93.87	55.70
Cr/ppm	50.35	108.00	162.95	152.86	120.04	135.80	64.12	123.75	107.71	87.19	175.00	180.51	64.71	125.29	48.53
Ni/ppm	84.14	152.54	173.95	171.74	120.96	115.12	181.13	163.96	193.55	106.53	230.38	197.75	118.61	159.99	40.76
Zn/ppm	343.91	237.69	268.83	165.76	56.94	300.98	262.16	211.12	188.09	145.16	68.79	69.53	83.90	73.61	95.71
Rb/ppm	70.37	41.09	87.36	85.78	29.80	63.89	89.54	69.76	73.09	76.97	67.03	40.77	70.04	35.96	102.03
Sr/ppm	180.53	518.22	214.81	202.28	531.18	266.16	176.19	269.06	233.01	250.37	246.38	436.40	313.41	398.90	195.04
Zr/ppm	67.54	66.89	97.69	103.97	63.31	75.77	99.98	75.76	84.95	73.97	87.74	71.49	82.74	59.32	70.60
Nb/ppm	7.18	6.38	10.21	11.10	7.15	6.82	9.76	9.64	7.75	9.33	8.27	7.83	8.84	7.11	10.80
Ba/ppm	1169.25	1100.94	969.30	974.54	673.22	621.16	715.85	632.01	713.19	674.06	711.13	606.84	918.17	895.86	803.57
Th/ppm	10.03	9.90	11.90	14.14	9.89	9.38	13.52	11.75	12.21	9.63	13.48	11.13	9.97	8.77	7.27
Mo/ppm	35.60	31.33	20.10	32.34	28.10	19.36	13.66	23.55	14.36	36.78	3.56	2.94	3.94	5.47	6.31
Co/ppm	6.10	8.11	22.33	21.97	14.63	20.36	33.11	19.14	22.85	26.82	22.31	9.85	11.32	6.36	8.47
Cd/ppm	10.36	6.12	2.03	1.96	2.66	1.55	1.36	2.10	1.03	0.66	0.35	0.21	0.35	0.31	0.26
V/Cr	8.78	4.12	3.09	2.21	1.70	3.34	3.22	2.79	3.11	2.64	1.16	0.72	2.04	1.91	3.52
V/(V + Ni)	0.84	0.74	0.51	0.43	0.40	0.57	0.30	0.45	0.40	0.45	0.24	0.17	0.30	0.37	0.58
V_{EF}	11.78	9.21	2.29	1.46	1.83	3.14	1.02	2.39	2.11	2.29	0.87	0.72	0.83	2.42	2.15
V/Ti	0.29	0.23	0.06	0.04	0.05	0.08	0.03	0.06	0.05	0.06	0.02	0.02	0.02	0.06	0.05
Zn/Ti	2290.70	1230.38	838.34	461.57	325.81	1561.84	850.90	949.13	757.10	937.56	207.21	313.32	349.42	474.42	921.61
Cd/Mo	0.29	0.20	0.10	0.06	0.09	0.08	0.10	0.09	0.07	0.02	0.10	0.07	0.09	0.06	0.04
Ba_{bio}/%	1005.00	889.60	618.49	581.66	482.02	410.34	378.79	388.67	441.40	504.68	347.95	364.07	655.49	726.12	689.96
Co × Mn/%	0.11	0.39	0.51	0.52	0.89	0.39	0.49	0.36	0.49	0.72	0.52	0.64	0.40	0.45	0.38
Mn/Sr/%	1.01	0.93	1.06	1.18	1.15	0.72	0.83	0.71	0.93	1.07	0.95	1.48	1.13	1.78	2.27

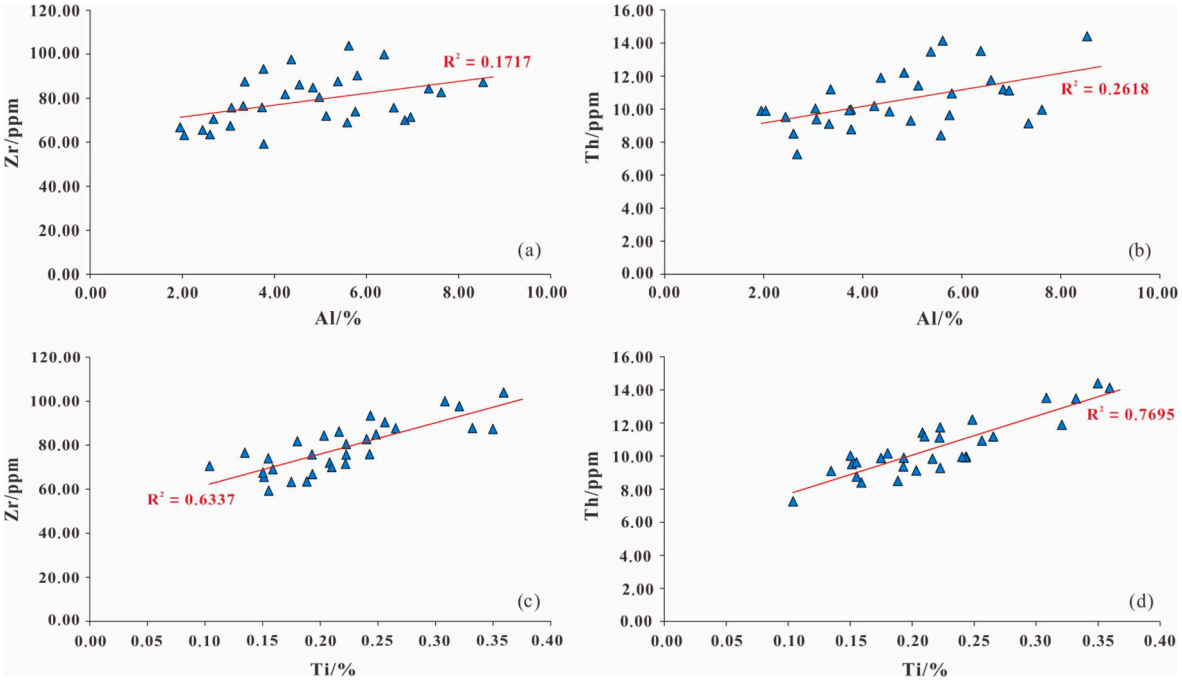

Fig. 10. The cross plots depict the relationships between Al and Zr (a), Al and Th (b), Ti and Zr (c), and Ti and Th (d).

is no significant change in Ti content. Meanwhile, the minor fluctuations observed among different samples are reflected in the changes in the content of Zr and Th. This indicates that there is a similar terrigenous detrital flux between Member 1 and Member 4, with no significant differences observed during the Eifelian period.

5.2. Evolution of paleoredox condition

The growth rate and morphology of goethite in framboidal pyrites differ in oxic and sulfidic marine environments (Raiswell and Berner, 1985). In oxidizing water columns, framboidal pyrites are only formed in sulfidic water of sediment pores (Wilkin et al., 1997). The slow supply of elements Fe and S results in framboidal pyrites with variable size and large individual diameter (Wignall et al., 2010). In sulfidic seawater, due to higher concentrations of elements Fe and S, pyrite microcrystals rapidly aggregate into framboidal pyrites. Suspended framboidal pyrites have been observed in water columns of the Black Sea (Gross, 1974), Kivu Lake (Degens et al., 1972), Kau Bay (Middelburg et al., 1988), Framvaren Strait (Skei, 1983), as well as modern lakes in Canada (Perry and Pedersen, 1993). Wilkin et al. (1996) found that the average diameter of framboidal pyrites in a sulfidic condition is 5.0 ± 1.7 μm, while in non-sulfidic water columns, it is 7.7 ± 4.1 μm. The pyrite framboids found in the Nabiao Formation are predominantly composed of small spherical microcrystals, suggesting a syngenetic origin (Figs. 8c–f). However, the clustered framboids observed in Member 4 (Figs. 8g and h) and the euhedral pyrites in Member 1 (Figs. 8a and b) are indicative of early diagenetic formation.

There are notable changes in both the quantity and size of framboidal pyrites in different members (Figs. 8 and 9). In Member 1, framboidal pyrites are almost absent (Figs. 8a and b). In sharp contrast, they are abundant in Member 2 and Member 3 (Figs. 8c–f), and those in Member 3 have the smallest average diameter, with the highest proportion of diameter smaller than 4 μm (Figs. 9a–f). This suggests that the sedimental environment of Member 2 and Member 3 is reductive, with Member 3 being more reductive. Although framboidal pyrites are also developed in Member 4, their quantity is significantly smaller than that of Member 3 (Figs. 8g and h). Additionally, the distribution of the framboidal pyrite diameter in Member 3 is much wider, with the diameter of many framboidal pyrites larger than 10 μm (Figs. 9g–i). Earlier research demonstrates that the average diameter of framboidal pyrites is related to paleoredox conditions (Wilkin et al., 1996; Liu et al., 2023; Xu et al., 2023). Consequently, Member 1 is associated with oxic conditions, Member 2 is characterized by prevailing dysoxic conditions, and Member 3 exhibits anoxic conditions that later transition into oxic-to-dysoxic conditions in Member 4.

In modern sulfidic environments, Mo concentration below 25 ppm reflects non-eutrophic condition, that between 25 and 100 ppm reflects intermittent eutrophication condition, and that above 100 ppm reflects permanent eutrophication condition (Tribovillard et al., 2006; Wu et al., 2020). In anoxic condition, U_{EF} and Mo_{EF} often exhibit synchronous changes. Algeo and Tribovillard (2009) proposed the use of U_{EF} and Mo_{EF} as indicators to reflect the redox conditions. The Mo_{EF} and U_{EF} show an increasing trend from Member 1 to Member 4, followed by a decreasing one. The pattern of U_{EF}-Mo_{EF} suggests that Member 1 is formed under oxic conditions and Member 4 formed under suboxic-to-anoxic conditions with less enrichment of Mo and U (Fig. 11). Compared to moderate enrichment of Mo and U observed in all samples of Member 2, 3 samples of Member 3 exhibit obvious enrichment of Mo and U. This reflects a transition from anoxic to euxinic conditions in water columns from Member 2 to Member 3 (Fig. 11). In contrast, the Mo/U ratio within restricted basins is lower than that of seawater due to limited Mo resupply, despite the stronger enrichment of Mo through the particulate shuttle process (Algeo and Tribovillard, 2009; Huang et al., 2023). As is shown in Fig. 11, the Mo/U ratios observed in the Nabiao Formation mostly fall within the “unrestricted marine trend".

Previous studies have suggested that multiple indicators are required to reflect paleoredox conditions. Trace elements such as U, V, and Ni, which are sensitive to redox conditions, have been widely used for identifying paleoredox conditions (Playter et al., 2017; LaGrange et al., 2020; Xu et al., 2023). Under reducing conditions, elements U, V, and Ni tend to enrich in sediments. Element Cr is chemically stable and thus is often used for standardization. The criteria for V/Cr ratios are <2.00 for oxic condition, 2.00–4.25 for dysoxic condition, and >4.25 for anoxic or euxinic environment (Wu et al., 2022). Furthermore, the ratios of V/(V + Ni) in the range of <0.46, 0.46–0.84, and >0.84 reflect oxic condition, dysoxic condition, and anoxic condition, respectively (Rimmer, 2004).

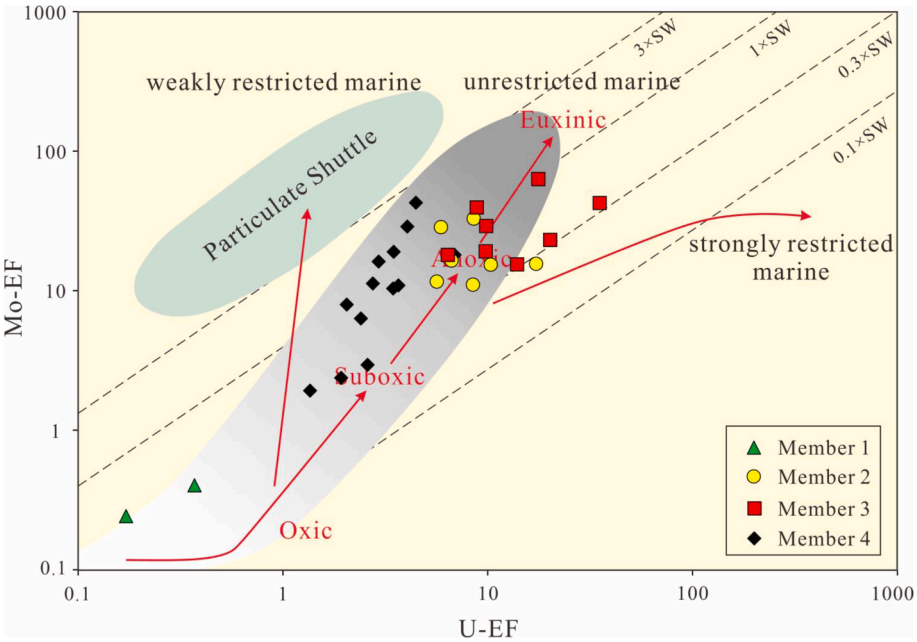

Fig. 11. Covariation pattern of Mo-EF versus U-EF (modified from Tribovillard et al., 2012; Liu et al., 2020; Wu et al., 2020).

The redox proxies (V/Cr, V/(V + Ni), V_{EF} and V/Ti) and $\delta^{13}C_{PDB}$ exhibit similar trends (Fig. 6). This suggests that the redox of water columns in the Nabiao Formation is greatly controlled by the relative sea-level change during the Eifelian period. The redox indicators show an oxic bottom water column in Member 1 (Fig. 6). Meanwhile, the limestone laminae and a large number of broken shells are in the calcareous mudstone (Figs. 5a and b). Following that, the marine redox state undergoes an upward change, leading to a progressive transformation into a dysoxic water column, with V/Cr ratios varying from 2.02 to 3.84 with an average of 2.87 (Table 3). The lithological boundary between mudstone and argillaceous limestone is one evidence of rapid rise in relative sea-level (Fig. 5c). In Member 3, ratios of V/Cr and V/(V + Ni) both indicate anoxic water columns (Fig. 6). Meanwhile, V_{EF} (mean 7.57) and V/Ti (mean 0.19) show relatively high values in the Nabiao Formation (Table 3). In Member 4, the values of redox proxies are reduced upwards, indicating a gradual evolution into oxic-dysoxic condition (Fig. 6). Therefore, the carbonate minerals can be seen in mudstone (Fig. 5i).

Previous studies have shown that the DOP_T values can serve as a reliable indicator of paleoredox condition (Qie et al., 2019). The DOP_T values are reported to be <0.42 for oxic condition, 0.42–0.75 for dysoxic condition, and >0.75 for anoxic condition (Appalachian et al., 2019). The DOP_T values of the Nabiao Formation samples range from 0.09 to 1.39 with an average of 0.59, indicating dysoxic-to-anoxic environment in the Eifelian period (Table 2). The values of DOP_T in Member 3 (mean 0.91) are generally higher than 0.59 (Table 2), indicating that the bottom water column of Member 3 has the lowest oxygen content in the Nabiao Formation.

The samples of the Nabiao Formation display evident vertical fluctuations in the redox state. Member 1 displays an oxic water column, as evidenced by the presence of redox indicators. With the rise of relative sea-level, Member 2 has dysoxic water columns and Member 3 has anoxic conditions. Member 4 experiences a transition from oxic to dysoxic conditions, which can be attributed to a minor decrease in sea-level.

5.3. Upwelling

The Youjiang Basin was located in the low latitude tropical neritic zone in Givetian, which was greatly influenced by the trade-wind zone (Fig. 1b) (Liu et al., 2015; Qie et al., 2019). The surface current of the trade-wind zone crosses the South China Sea and enters the Jinsha River Ocean to the west, forming the westward surface current in the South China Sea and the eastward upwelling current at the bottom of the sea (Chen et al., 2001; Ma et al., 2009b). The upwelling occurring along contemporary continental margins, such as the coasts of Peru and Namibia, exerts dual beneficial effects on the enrichment of organic matter (Wu et al., 2022). By delivering a substantial influx of nutrients, the upwelling facilitates the proliferation of organisms. The sediments after biological death contribute to an increase in the proportion of biogenic silica in silicate minerals, ensuring an adequate source of organic matter (Parrish, 1982; Kametaka et al., 2005). Simultaneously, the decomposition of organic matter consumes a substantial quantity of oxygen within a water column, fostering the formation of oxygen-minimum zones at the continental margins (Böning et al., 2004; Scholz et al., 2011). The rate of oxygen consumed by organic matter degradation is greater than that of oxygen transported from surface water columns to deeper water columns, which also leads to an anoxic environment in restricted basins (Wu et al., 2020; Hou et al., 2022; Cao et al., 2023).

Generally, sediments are relatively enriched in elements Cd and Mo through upwelling, and less enriched in Co and Mn (Böning et al., 2004). Böning et al. (2004) and Sweere et al. (2016) proposed that the geochemical indexes of Cd/Mo and Co × Mn can be used to distinguish the formation modes of anoxic environment between upwelling and restricted basins. Under the influence of upwelling, the ratios of Cd/Mo and Co × Mn in sediments are usually considered to be more than 0.1 and less than 0.4, respectively (Wang et al., 2019; Hou et al., 2022; Cao et al., 2023). During the deposition of Member 3, the average values of Cd/Mo and Co × Mn are 0.24 and 0.26, respectively (Fig. 6; Table 3), indicating the presence of a robust coastal upwelling environment.

Organic matter-silica-mudstone assemblages and rhythmic layering are usually developed in upwelling sediments (Wu et al., 2022). The rhythmic layering of shale and siliceous shale are shown by the upwelling sediments in the Lower Yangtze Area (Kametaka et al., 2005; Wang et al., 2017). The siliceous mudstone (Figs. 5d and e), siliceous shale (Figs. 5f and g) and carbonaceous mudstone (Fig. 5h) are deposited in Member 3 of the Nabiao Formation. The lithology of marine sediments can be controlled by the upwelling intensity and development frequency (Chen et al., 2001). The upwelling indicators (Cd/Mo and Co

× Mn) show that the carbonaceous mudstone (M-3) is developed during a weak upwelling period (Fig. 5h), while the siliceous mudstone (S-3) and siliceous shale (S-2) are developed during a strong upwelling period (Figs. 5d–g). Compared with the mudstone of other members, the carbonaceous mudstone, siliceous mudstone and siliceous shale of Member 3 are deposited in water columns characterized by higher productivity and stronger reducing conditions (Fig. 6). Consequently, the accumulation of organic matter can be linked to enhanced productivity and increased oxygen depletion in water columns, which is caused by upwelling.

In addition, the phosphorus nodules are deposited in shale and a large quantity of tentaculites is developed in limestone of the Middle Devonian formation in Debao City and Chongzuo City (Yu et al., 2021). The phosphorus-bearing mudstone with tentaculites is deposited in the Middle Devonian formation of Hechi City (Gong et al., 1997). Siliceous masses and layers are developed in limestone of the bottom of the Middle Devonian formation (Chen et al., 2001). It can be seen that upwelling developed in large quantities during the Middle Devonian is one of the important factors controlling the lithology and organic matter enrichment of the sediments of the Nabiao Formation in the Youjiang Basin.

5.4. Paleoproductivity

Productivity is the ability of an organism to generate organic matter from water, carbon dioxide, and inorganic salt through photosynthesis and chemical synthesis (Li et al., 2017; Xiao et al., 2021). Although the primary productivity of surface marine water is influenced by various factors such as sunlight duration, water temperature, and salinity, the fundamental controlling factors are the content of various nutrients, including elements Ba, Zn, and P (Schoepfer et al., 2015; Wu et al., 2020; Hou et al., 2022).

Element Ba is primarily enriched in marine sediments in the form of barite. Barite is easily buried during sedimentation processes (with more than 30% of barite being buried) (Dymond and Lyle., 1992), and remains stable during diagenesis. Therefore, Ba_{bio} can serve as an indicator of paleoproductivity, reflecting productivity of ancient water columns. In Member 1, the calculated average Ba_{bio} content based on the equation is relatively low (Table 3), which is in line with the values observed for Si_{bio} and Zn/Ti ratios (Fig. 6). The Ba_{bio} content of Member 2 and Member 3 is generally higher compared to that of the samples from the Nabiao Formation, with the highest Ba_{bio} content of Member 3 (mean 920.87%) (Table 3). Member 4 exhibits an average Ba_{bio} content of 506.89%, indicating a decrease in productivity compared to Member 3.

Silicon in sediments is primarily preserved in detrital quartz or biogenic quartz (Kidder and Erwin, 2001). In marine mudstone, planktonic organisms play a dual role as the primary contributors to primary productivity in the ocean and the primary source of biogenic silica (Wu et al., 2020). Therefore, Si_{bio} content can serve as an indicator for evaluating productivity levels (Khan et al., 2019). The supply of biogenic silica is greatly influenced by the biological activities and the presence of volcanic hydrothermal fluids (Wang et al., 2017; Xiao et al., 2021; Cao et al., 2023). The Al–Fe–Mn ternary diagram indicates no significant hydrothermal activity in the Eifelian period (Fig. 12). Therefore, the Si_{bio} content of samples can accurately reflect the paleoproductivity level of the Nabiao Formation (Fig. 6; Table 2).

There is a similar trend in the content variation of Si_{bio} and Ba_{bio} (Fig. 6). The Si_{bio} content is extremely low in Member 1, suggesting poor productivity (Table 2). This may be related to the fact that the producers (planktonic algae, etc.) are hardly developed (Figs. 7j–l). Member 3 has the highest Si_{bio} content (mean 10.26%), higher than that of Member 2 (mean 7.39%), and much higher than that of Member 4 (4.86%) (Table 2). This may be related to the bloom of algae, as shown in Fig. 7g. The Si_{bio} content increases to the maximum in Member 3 (up to 19.75%) and then decreases in Member 4. This trend is consistent with the upwelling intensity (Fig. 6). It can be seen that upwelling is the key factor for the much higher productivity of Member 3 than that of other members.

Previous researches have confirmed the effectiveness of using elements Ni and Zn as reliable indicators of paleoproductivity due to their notable enrichment in organic matter in the form of complexes subsequent to the decay of organic materials, as proposed by Tribovillard et al. (2006) and Aigbadon et al. (2022). The ratio of Zn/Ti removes the

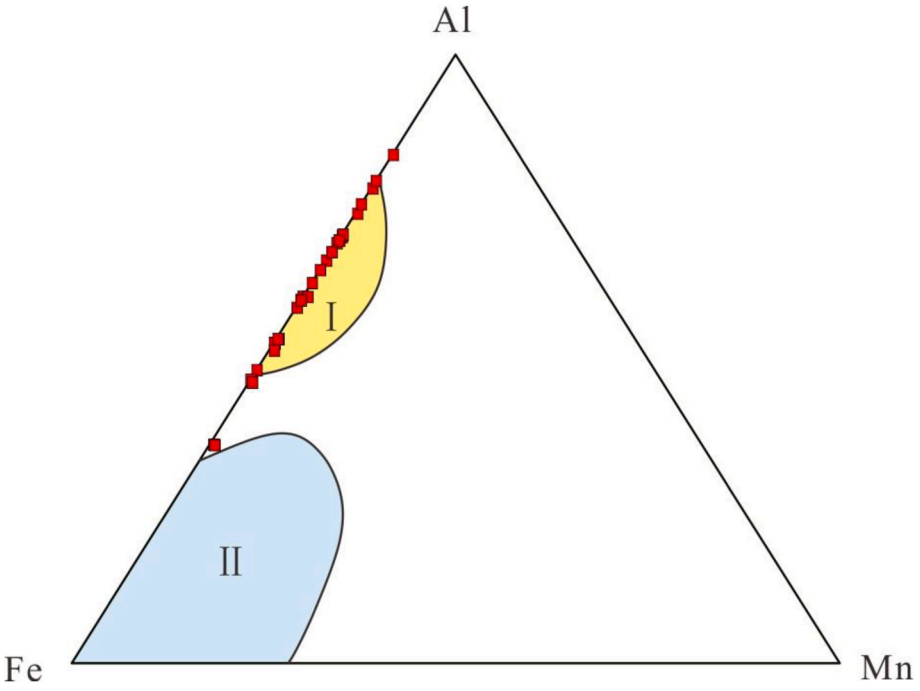

Fig. 12. Ternary diagram of Al–Fe–Mn illustrating the Nabiao Formation samples of Well ND falling into the biogenic and non-hydrothermal area. I: biogenic and non-hydrothermal sediments, II: hydrothermal sediments. Hydrothermal and non-hydrothermal fields are from Wang et al. (2017).

influence of terrestrial debris to better reflect paleoocean productivity. As shown in Fig. 6, the Zn/Ti values of the Nabiao Formation show a trend of initially rising and subsequently declining. The algae flourish and reach the peak productivity under the influence of upwelling in Member 3 (Figs. 6 and 7g). With the weakening of transgression in Member 4, the degree of algal development decreases (Fig. 7i), and the productivity decreases at the same time (Fig. 6).

5.5. Characteristics of controlling factors for organic matter accumulation

The enrichment of organic matter is a multifaceted physicochemical process governed by various factors, such as redox condition, productivity, and the input of terrestrial detritus (Cao et al., 2023; Chen et al., 2023). Even during the same sedimentary period, the dominant controlling factors of organic matter enrichment can undergo changes as a result of geological events and other factors (Sageman et al., 2003; Xiao et al., 2021).

In Member 1, the relative sea-level is low (Fig. 6). As shown in Figs. 7j–l, the organic matter is predominantly derived from terrigenous organic components, which are the primary factors in its composition. The oxygen-rich water does not have a positive effect on the preservation of organic matter. A small number of planktonic algae cause the majority of silicate minerals to come from terrigenous debris (Table 2). As a result, the calculated value of Si_{bio} is less than 0, and values of Ba_{bio} and Si_{bio} have no contribution to TOC content (Figs. 13c and d). Under the conditions of oxygen-rich water columns and low productivity, the degree of organic matter enrichment is low in Member 1 (Figs. 13e and f).

The redox fingerprints suggest that Member 2 is deposited in dysoxic water columns (Fig. 6). The V/(V + Ni) ratio shows a strong positive correlation with TOC content, with an R^2 value of 86.58%. Additionally, there is a positive correlation between V_{EF} and TOC content, with an R^2 value of 51.46%, as depicted in Figs. 13e and f. It can be seen that reduction conditions play an active role in the preservation of organic matter, and also promote the enrichment of organic matter. There is no correlation between TOC and the content of Ti and Zr, indicating that the input of terrigenous detritus has almost no effect on the enrichment of organic matter (Figs. 13a and b). The figures (Figs. 13c and d) demonstrate that the paleoproductivity proxies Ba_{bio} and Si_{bio} exhibit a positive correlation with TOC content, with R^2 values of 52.20% and 32.65%, respectively. These findings indicate that an increase in primary productivity contributes to some extent to the enrichment of organic matter. Compared to Member 1, the significant increase in productivity of Member 2 is attributed to the development of a large number of planktonic algae (Figs. 7b, j–l). Overall, the dysoxic environment preserves the organic matter produced by planktonic algae and allows for organic matter enrichment of Member 2.

In Member 3, the redox indicators exhibit no significant correlation

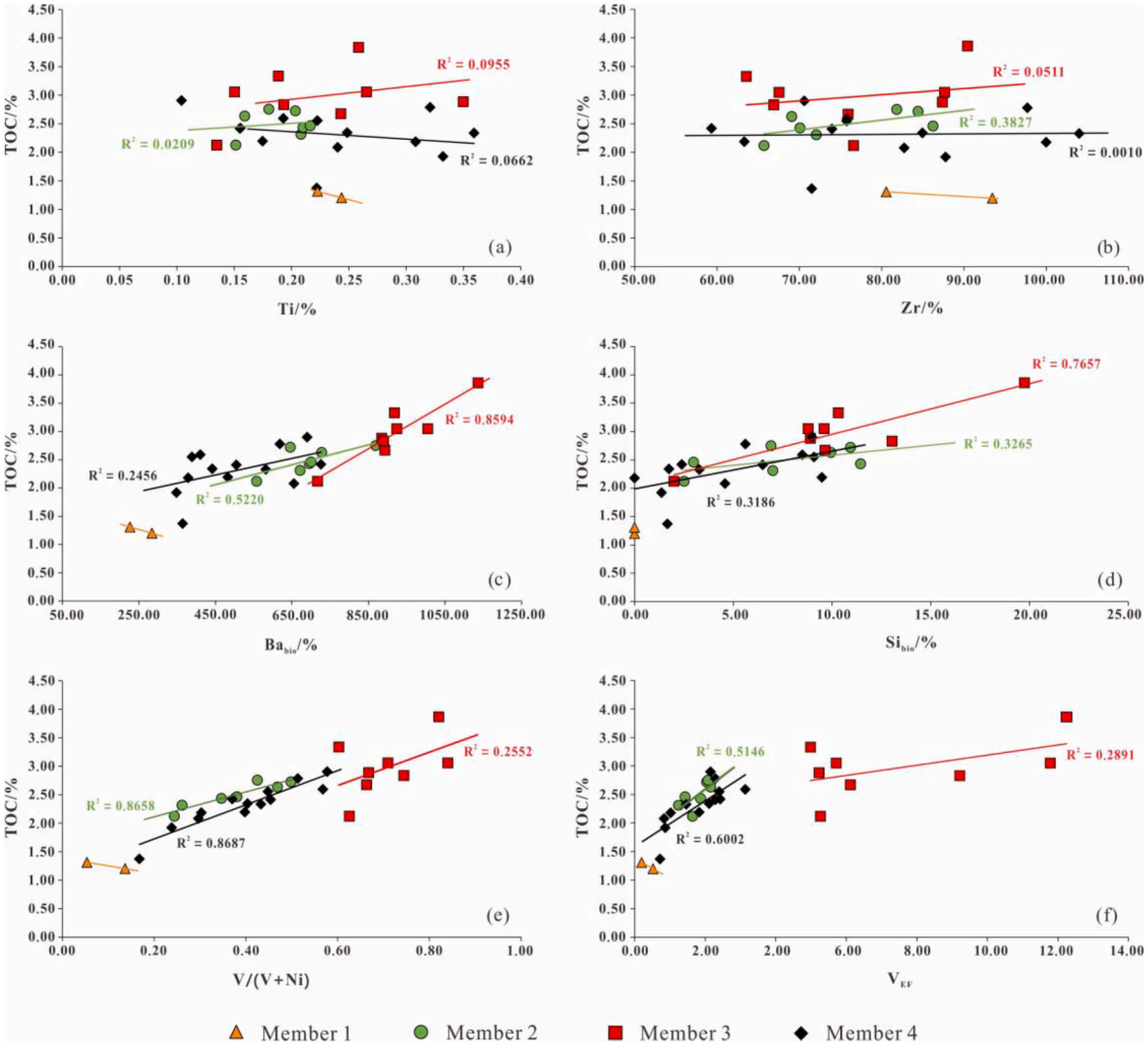

Fig. 13. Cross plots of Ti (a), Zr (b), Ba_{bio} (c), Si_{bio} (d), V/(V + Ni) (e) and V_{EF} (f) versus TOC content.

with TOC content and V/(V + Ni) and V_{EF} ratios with $R^2 = 25.52\%$ and 28.91%, respectively (Figs. 13e and f). The Ba_{bio} and Si_{bio} exhibit a strongly positive correlation with TOC content with $R^2 = 85.94\%$ and $R^2 = 76.57\%$, respectively (Figs. 13c and d). This indicates that the enrichment of organic matter in Member 3 is predominantly attributed to primary productivity (Fig. 6). The increase in productivity of Member 3 is attributed to the surface water bloom of marine organisms, such as planktonic algae, etc., caused by nutrient-laden upwelling (Fig. 7g). In addition, the terrestrial detrital input has no apparent influence on the organic matter enrichment of Member 3. Therefore, the enrichment of organic matter in Member 3 is attributed to upwelling.

In Member 4, the sea-level fluctuation decreases, as shown by the change of $\delta^{13}C_{PDB}$ values (Fig. 6). The archipelago paleogeography to some extent limits the exchange of bottom water and open ocean, resulting in the weakening of upwelling (Fig. 6). As a result, the contribution of productivity to organic matter enrichment is reduced compared to Member 3 (Fig. 6). As shown in Figs. 13e and f, the dysoxic water columns of the basin become the primary factor driving the accumulation of organic matter, while productivity only promotes organic matter enrichment to a certain extent. TOC content is not affected by terrigenous detrital flux and shows almost no correlation with Ti and Zr content (Figs. 13a and b). In summary, the dysoxic environment protects organic matter from depletion.

5.6. Model of organic matter accumulation

During the early Eifelian period, a momentous tectonic uplift was in full swing in the South China coastal waters. This significant event brought about the deposition of the Nabiao Formation in a shallow water column, as depicted in Fig. 6 (Qie et al., 2019). The expansion of the platform range was accompanied by a shallower water column in the basin. Furthermore, the Eifelian limestone shrouded some reefs deposited in the early Devonian (Zeng et al., 1995; Ma et al., 2009b). As shown in Member 1 of Well ND, calcareous mudstone and argillaceous limestone are deposited (Figs. 5a–c). The presence of abundant vitrinite and inertinite particles indicates a significant contribution of organic matter derived from terrestrial sources (Figs. 7j–l). The less algae lead to the emergence of low productivity. Meanwhile, oxygen-rich water columns intensifies the decomposition and consumption of organic matter, ultimately resulting in the failure of organic matter enrichment (Fig. 14a).

The Chotec Event represents a global sea-level rise and ocean anoxia event characterized by the burial of a large amount of organic matter and apparent turnover of major marine biota in the ocean (McGhee et al., 2013; Kabanov et al., 2023). In stage 2, influenced by Chotec Event in the South China, the sea-level deepened rapidly (Fig. 6). The water column of the basin was relatively high, and the mudstone was deposited (Fig. 5c). The rising relative sea-level and deepening water depth reduced the possibility of oxygenated surface water mixing with the sediment-water interface. Consequently, sediments were deposited in dysoxic water columns, better preserving the organic matter (Fig. 6). Moreover, the rising relative sea-level disrupted the barrier of the platform, and ultimately loosened its constraints related to the exchange of basin water with seawater. The development of planktonic algae led to increased productivity of Member 2 (Fig. 7h). In summary, the high TOC content of mudstone is mostly attributed to the dysoxic environment (Fig. 14b).

With the persistent transgression, the basin water gradually deepened into an anoxic bottom basin water environment (Fig. 6) (Qie et al., 2019). At the same time, the sediments were less susceptible to the influence of terrestrial debris (Fig. 6). The Youjiang Basin during the Eifelian period was at low to middle latitudes (Fig. 1b), with a relatively warm and humid climate, which was favorable to zooplankton growth (Fig. 7g). Under the influence of atmospheric circulation, submarine upwelling was frequent. The upwelling brought abundant nutrients from deep seawater into basin water. The abundance of nutrients fostered the proliferation of siliceous organisms, leading to a substantial increase in primary productivity. As shown in Figs. 5e–h, the higher the upwelling intensity, the more silicate minerals deposited. At the same time, the excessive organic matter generated from this process was transformed to bottom water, leading to the consumption of free oxygen in water columns and eventually exacerbating anoxic bottom-water conditions. In conclusion, the TOC content of Member 3 is heavily dependent on the intensity of upwelling (Fig. 14c).

In stage 4, there was a relative sea-level drop (Fig. 6) (Walliser, 1996; Lu et al., 2016). The bottom water of the basin transitioned from dysoxic to anoxic (Fig. 6). The upward decrease in the abundance of phytoplankton and the upward increase in the vitrinite component both indicate a gradual decrease in productivity in stage 4 (Fig. 7i). The organic matter of Member 4 is composed of autochthonous and terrestrial organic matter (Appendix 1). The influx of terrigenous detrital minerals have negligible effects on the enrichment of organic matter (Figs. 13a and b). Although the Kacak Event caused the relative sea-level of the Youjiang Basin to rise, the transgression intensity during the late Eifelian period was not strong (Fig. 6). Therefore, under the control of the mainly dysoxic condition, the TOC content of Member 4 is relatively low (Fig. 14d).

5.7. Implications for shale gas exploration

Under the influence of transgression, a set of fine-grained sediments, mainly mudstone, siliceous mudstone and siliceous shale, of the Middle Devonian Nabiao Formation are deposited in the basin. Well ND is the only well in the study area that was drilled through the complete Nabian Formation and continuously cored. The study of mineralogical, petrological and geochemical characteristics of 30 core samples from Well ND helps to objectively evaluate the hydrocarbon potential of the sediments in the Nabiao Formation, providing a basis for the selection and evaluation of shale gas exploration.

The organic enrichment of Member 1 is low under the conditions of oxygen-enriched water columns and low productivity. The calcareous mudstone ($TOC_{average}$= 1.20 %) and argillaceous limestone ($TOC_{average}$= 1.31 %) do not have hydrocarbon generation potential. The significant relative sea-level rise caused by the Chotec transgression contributes to the enrichment of organic matter. Therefore, the mudstone ($TOC_{average}$= 2.49 %) of Member 2 has hydrocarbon generation potential. In Member 3, carbonaceous mudstone ($TOC_{average}$= 2.88 %) is deposited in a weak upwelling, while siliceous mudstone ($TOC_{average}$= 2.80 %) and siliceous shale ($TOC_{average}$= 3.46 %) are developed in a strong upwelling. Compared with the mudstone of Member 2 and Member 4, the sediments of Member 3 have significantly higher TOC content and stronger hydrocarbon generation potential. In Member 4, the enrichment of organic matter in mudstone ($TOC_{average}$= 2.31 %) has been reduced by the relative sea-level drop.

In general, TOC content of siliceous mudstone, siliceous shale and carbonaceous mudstone in the basin is generally high, indicating strong hydrocarbon generation potential. Therefore, Member 3 can be prioritized as a crucial section for shale gas exploration in the Youjiang Basin.

6. Conclusions

The study aims to assess the impact of archipelago paleogeography and transgression on organic matter accumulation in the Nabiao Formation by incorporating sedimentological, petrographic, mineralogical, and geochemical analyses. The conclusions are as follows:

(1) The argillaceous limestone and calcareous mudstone with low TOC content belong to mixed shale lithofacies in Member 1. In Member 2, the mudstone has relatively high TOC content. The upper part belongs to silica-rich argillaceous shale lithofacies and the lower part belongs to argillaceous/siliceous mixed shale lithofacies. Member 3 has high TOC content. The siliceous mudstone belongs to clay-rich siliceous shale lithofacies, the

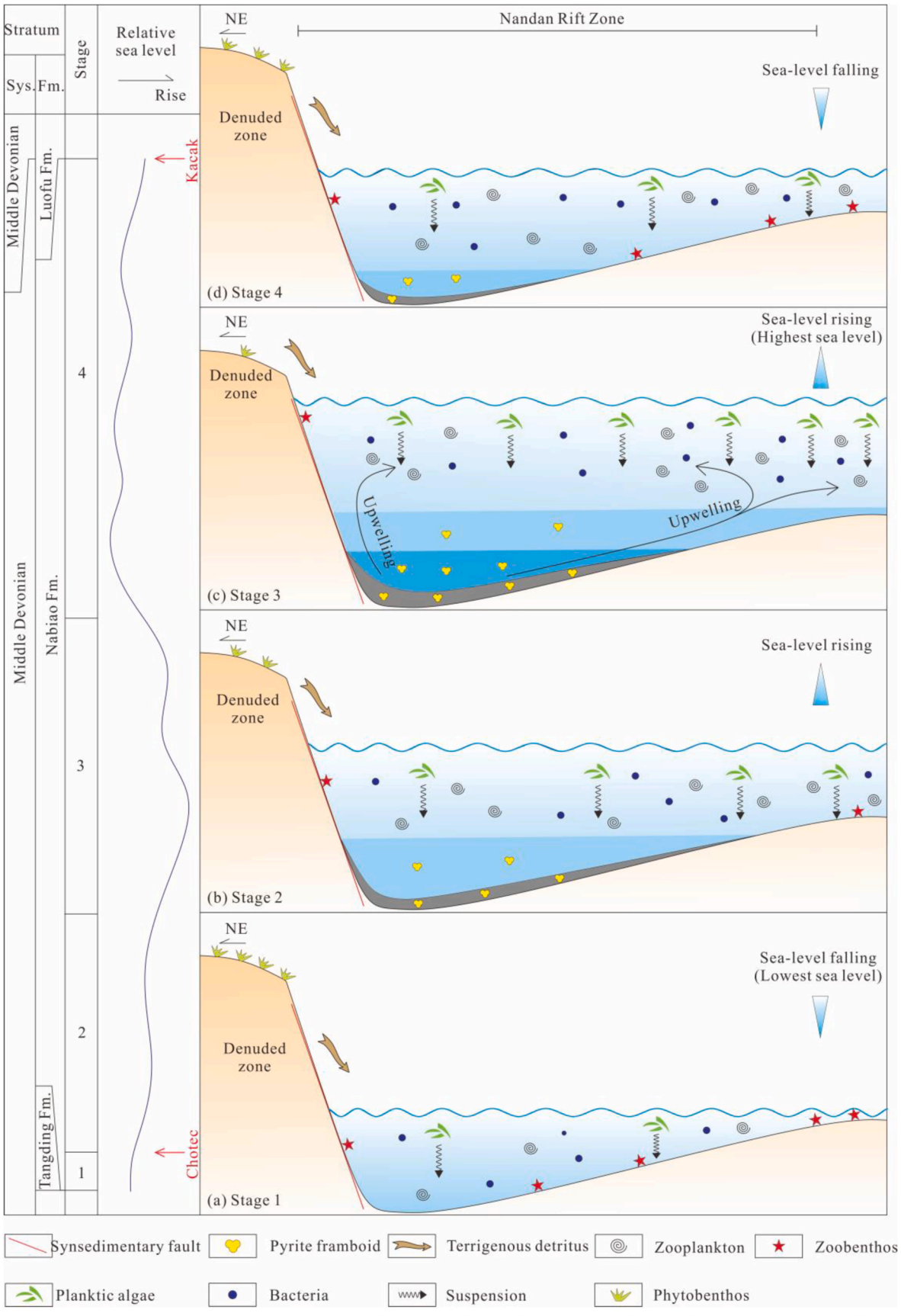

Fig. 14. Model of organic matter accumulation in the Nabiao Formation sediments of the Youjiang Basin during the deposition of Stage I (a), Stage II (b), Stage III (c), and Stage IV (d); in this model, the archipelago paleogeography and transgression control the accumulation rate of organic matter through changes in marine paleoredox conditions, paleoproductivity, and terrestrial detrital influx.

siliceous shale belongs to mixed siliceous shale lithofacies, and the mudstone belongs to mixed shale lithofacies. In Member 4, the mudstone with relatively low TOC content mainly belongs to argillaceous/siliceous mixed shale lithofacies.

(2) The lithology of Member 3 is controlled by the intensity and development frequency of upwelling. During the weak upwelling period, the carbonaceous mudstone is deposited, while the siliceous mudstone and siliceous shale are developed during the strong upwelling period.

(3) The accumulation model of organic matter in Nabiao mudstone can be divided into four stages. In stage 1, the low TOC content is caused by oxic water columns and low productivity. The organic matter enrichment is attributed to the dysoxic bottom water columns caused by the Chotec Event in stage 2. In stage 3, the organic matter enrichment is mainly controlled by upwelling-driven paleoproductivity. In stage 4, the organic matter accumulation is the result of the dysoxic conditions. The terrigenous detrital flux has no significant impact on the enrichment of organic matter in the Nabiao Formation.

(4) The Chotec Event is more conducive to the organic matter enrichment in the Nabian Formation mudstone than the Kacak Event. The Chotec Event caused the relative sea-level of Member 2 to rise rapidly and the basin bottom water to quickly change into dysoxic conditions. Powerful and persistent transgression of Member 3 enhanced the exchange degree of basin bottom water with the open sea, so that the upwelling brought marine nutrients into the basin surface water columns, promoting more productive and less bottom water columns in the basin. The Kacak event only caused a slight increase in relative sea-level of the basin at the end of the Eifelian period, so it had no significant contribution to organic matter enrichment.

Declaration of competing interest

The authors declare that they have no known competing financial interests or personal relationships that could have appeared to influence the work reported in this paper.

Data availability

Data will be made available on request.

Acknowledgements

We thank anonymous reviewers for their constructive comments that greatly improve this manuscript. This study is jointly supported by the China Scholarship Council (CSC) (202206410022), the National Natural Science Foundation of China (No. 41672134), the National Natural Science Foundation of China (No. 42202121), and the fellowship of China Postdoctoral Science Foundation (No. 2022M712952).

Appendix 1

Kerogen maceral analysis results of each sample in the Nabiao Formation.

Sample No.	Depth/m	Member	Sapropelinite/%	Exinite/%	Vitrinite/%	Inertinite/%	TI	Kerogen type
No.1	809.90	1	56.00	10.00	29.00	5.00	34.25	II_2
No.2	806.10	1	60.00	9.00	25.00	6.00	39.75	II_2
No.3	801.00	2	72.00	2.00	26.00	0.00	53.50	II_1
No.4	797.00	2	93.00	5.00	2.00	0.00	94.00	I
No.5	789.20	2	90.00	1.00	9.00	0.00	83.75	I
No.6	782.90	2	55.00	22.00	23.00	0.00	48.75	II_1
No.7	776.80	2	49.00	25.00	26.00	0.00	42.00	II_1
No.8	769.00	2	59.00	19.00	22.00	0.00	52.00	II_1
No.9	761.20	2	89.00	1.00	10.00	0.00	82.00	I
No.10	755.00	3	93.00	0.00	7.00	0.00	87.75	I
No.11	747.10	3	94.00	0.00	6.00	0.00	89.50	I
No.12	739.10	3	97.00	0.00	3.00	0.00	94.75	I
No.13	730.90	3	95.00	0.00	5.00	0.00	91.25	I
No.14	721.10	3	97.00	0.00	3.00	0.00	94.75	I
No.15	713.10	3	95.00	0.00	5.00	0.00	91.25	I
No.16	705.10	3	93.00	0.00	7.00	0.00	87.75	I
No.17	697.10	3	89.00	2.00	9.00	0.00	83.25	I
No.18	689.10	4	75.00	3.00	22.00	0.00	60.00	II_1
No.19	681.10	4	77.00	2.00	21.00	0.00	62.25	II_1
No.20	673.10	4	70.00	1.00	29.00	0.00	48.75	II_1
No.21	665.10	4	90.00	0.00	10.00	0.00	82.50	I
No.22	658.70	4	65.00	4.00	31.00	0.00	43.75	II_1
No.23	654.70	4	77.00	2.00	21.00	0.00	62.25	II_1
No.24	647.90	4	69.00	6.00	25.00	0.00	53.25	II_1
No.25	643.10	4	69.00	1.00	30.00	0.00	47.00	II_1
No.26	635.10	4	73.00	3.00	24.00	0.00	56.50	II_1
No.27	627.10	4	76.00	2.00	22.00	0.00	60.50	II_1
No.28	619.10	4	93.00	1.00	6.00	0.00	89.00	I
No.29	611.10	4	86.00	5.00	9.00	0.00	81.75	I
No.30	607.90	4	75.00	2.00	23.00	0.00	58.75	II_1

References

Abouelresh, M.O., Slatt, R.M., 2012. Lithofacies and sequence stratigraphy of the barnett shale in east-central fort worth basin, Texas. AAPG (Am. Assoc. Pet. Geol.) Bull. 96, 1–22.

Aigbadon, G.O., Odoma, A.N., Obasi, I.A., Christopher, S.D., Nanfa, C.A., Mu'awiya, B. A., Akakuru, O.C., 2022. Hydrocarbon prospectivity of the southern Bida and northern Anambra basins, Nigeria using palynological and geochemical studies. Geosyst. Geoenviron. 1 (4), 100103.

Algeo, T.J., Hinnov, L., Moser, J., Maynard, J.B., Elswick, E., Kuwahara, K., Sano, H., 2010. Changes in productivity and redox conditions in the Panthalassic Ocean during the latest Permian. Geology 38, 187–190.

Algeo, T.J., Maynard, J.B., 2004. Trace-element behavior and redox facies in core shales of Upper Pennsylvanian Kansas-type cyclothems. Chem. Geol. 206, 289–318.

Algeo, T.J., Tribovillard, N., 2009. Environmental analysis of paleoceanographic systems based on molybdenum–uranium covariation. Chem. Geol. 268 (3-4), 211–225.

Aplin, A.C., Macquaker, J.H., 2011. Mudstone diversity: origin and implications for source, seal, and reservoir properties in petroleum systems. AAPG Bull. 95, 2031–2059.

Appalachian, C., Liu, J., Algeo, T.J., Jaminski, J., Kuhn, T., Joachimski, M.M., 2019. Evaluation of high-frequency paleoenvironmental variation using an optimized cyclostratigraphic framework: example for C-S-Fe analysis of. Chem. Geol. 525, 303–320.

Blattmann, T.M., Liu, Z., Zhang, Y., Zhao, Y., Haghipour, N., Montluçon, D.B., Plotze, M., Eglinton, T.I., 2019. Mineralogical control on the fate of continentally derived organic matter in the ocean. Science 366, 742–745.

Böning, P., Brumsack, H.J., Böttcher, M.E., Schnetger, B., Kriete, C., Kallmeyer, J., Borchers, S.L., 2004. Geochemistry of Peruvian near-surface sediments. Geochem. Cosmochim. Acta 68, 4429–4451.

Calvert, S.E., Pedersen, T.F., 2007. Elemental proxies for palaeoclimatic and palaeoceanographic variability in marine sediments: interpretation and application. Develop. Marine Geol. 1, 567–644.

Cao, H.S., Wang, Z.Y., Dong, L.F., Xiao, Y.C., Hu, L.M., Chen, F.J., Wei, K., Chen, C.Q., Song, Z.G., Wu, L., 2023. Influence of hydrothermal and upwelling events on organic matter accumulation in the gas-bearing lower Cambrian shales of the middle Yangtze Block, South China. Mar. Petrol. Geol., 106373

Chabalala, V.P., Wagner, N., Malumbazo, N., Eble, C.F., 2020. Geochemistry and organic petrology of the permian whitehill formation, Karoo Basin (RSA) and the Devonian/Carboniferous shale of the Appalachian Basin (USA). Int. J. Coal Geol. 232, 103612.

Chen, D., Tucker, M.E., Zhu, J., Jiang, M., 2001. Carbonate sedimentation in a starved pull-apart basin, middle to late devonian, southern guilin, South China. Basin Res. 13 (2), 141–167.

Chen, W.Z., Tian, J.C., Lin, X.B., Liang, Q.S., Wang, X., Yi, D.X., Li, Y.Y., 2023. Climate fluctuations during the Ordovician-Silurian transition period in South China: implications for paleoenvironmental evolution and organic matter enrichment. Palaeogeogr. Palaeoclimatol. Palaeoecol. 613, 111411.

Cheng, Y.S., 2011. Ore-controlling characteristics of Devonian stratum in the Dachang Sn ore-field, Guangxi (south China). Procedia Earth Planetary Sci. 2, 28–33.

Degens, E.T., Okada, H., Honjo, S., Hathaway, J.C., 1972. Microcrystalline sphalerite in resin globules suspended in lake Kivu, east africa. Miner. Deposita 7, 1–12.

Dymond, J., Lyle, M., 1992. Particle fluxes in the ocean and implications for sources and preservation of ocean and sediments. In: Geomaterial Fluxes, Glacial to Recentedited by W.W.Hay. National Research Council National Academy of Sciences Press, Washington, D.C (in press).

Elbra, T., Soták, J., Kdýr, Š., Kohout, T., Schnabl, P., Skála, R., Pruner, P., 2023. Cretaceous to Palaeogene boundary events and palaeoenvironmental responses across pelagic sequences of the Žilina core section, Slovakia: rock magnetic, biotic, and geochemical characterization. Palaeogeogr. Palaeoclimatol. Palaeoecol., 111682

Golonka, J., 2002. Plate-Tectonic Maps of the Phanerozoic. Phanerozoic Reef Patterns.

Gong, Y.M., Wu, Y., Du, Y.S., Feng, Q.L., Liu, B.P., 1997. Devonian Sea-level change rhythms in South China and coupling relationships among the earth-spheres. Acta Geol. Sinica-Eng. Ed. 71 (4), 370–385.

Gradstein, F.M., 2020. Evolution and biostratigraphy. In: Geologic Time Scale 2020. Elsevier, pp. 35–137.

Gross, M.G., 1974. The Black Sea-Geology, Chemistry, and Biology. American Association of Petroleum Geologists, Tulsa, Oklahoma, pp. 1016–1017.

Heath, M.N., Cramer, B.D., Stolfus, B.M., Barnes, G.L., Clark, R.J., Day, J.E., Barnett, B. A., Witzke, B.J., Hogancamp, N.J., Tassier-Surine, S., 2021. Chemoautotrophy as the driver of decoupled organic and carbonate carbon isotope records at the onset of the Hangenberg (Devonian-Carboniferous Boundary) Oceanic Anoxic Event. Palaeogeogr. Palaeoclimatol. Palaeoecol. 577, 110540.

Hou, H.H., Shao, L.Y., Li, Y.H., Liu, L., Liang, G.D., Zhang, W.L., Wang, X.T., Wang, W.C., 2022. Effect of paleoclimate and paleoenvironment on organic matter accumulation in lacustrine shale: constraints from lithofacies and element geochemistry in the northern Qaidam Basin, NW China. J. Petrol. Sci. Eng. 208, 109350.

House, M.R., 2002. Strength, timing, setting and cause of mid-Palaeozoic extinctions. Palaeogeogr. Palaeoclimatol. Palaeoecol. 181, 5–25.

Hu, D.P., Zhang, X.L., Li, M.H., Xu, Y.L., Shen, Y.N., 2021. Carbon isotope ($\delta^{13}C_{carb}$) stratigraphy of the lower-upper ordovician of the Yangtze platform, South China: implications for global correlation and the great ordovician biodiversification event (GOBE). Global Planet. Change 203, 103546.

Huang, J.Y., Liang, K., Wang, Y., Liao, W.H., Guo, W., Kershaw, S., Jeon, J., Lq, Song, J. J., Ma, J.Y., Li, Y., B, T., Tian, Y., Wang, Y.J., Wang, Y., Ma, J.X., Luo, M., Qie, W.K., 2020. The Jiwozhai patch reef: a palaeobiodiversity hotspot in middle Givetian (Devonian) of South China. Palaeogeogr. Palaeoclimatol. Palaeoecol. 556.

Huang, Z.S., Li, Z.Q., Zhu, Y.Q., Shi, W.R., Li, Y., Li, Y., Huang, Y.J., Young, S., 2023. Organic matter accumulation of the upper triassic Ma'antang shales in the longmenshan foreland basin (western Sichuan, China). Sediment. Geol. 444, 106318.

International Committee for Coal and Organic Petrology (ICCP), 1998. The new vitrinite classification (ICCP systems 1994). Fuel 77, 349–358.

International Committee for Coal and Organic Petrology (ICCP), 2001. The new inertinite classification (ICCP system 1994). Fuel 80 (4), 459–471.

Kabanov, P., Hauck, T.E., Gouwy, S.A., Grasby, S.E., van der Boon, A., 2023. Oceanic anoxic events, marine photic-zone euxinia, and controversy of sea-level fluctuations during the Middle-Late Devonian. Earth Sci. Rev., 104415

Kametaka, M., Takebe, M., Nagai, H., Zhu, S.Z., Takayanagi, Y., 2005. Sedimentary environments of the Middle Permian phosphorite–chert complex from the northeastern Yangtze platform, China; the Gufeng Formation: a continental shelf radiolarian chert. Sediment. Geol. 174 (3-4), 197–222.

Khan, M.Z., Feng, Q.L., Zhang, K., Guo, W., 2019. Biogenic silica and organic carbon fluxes provide evidence of enhanced marine productivity in the Upper Ordovician-Lower Silurian of South China. Palaeogeogr. Palaeoclimatol. Palaeoecol. 534 (15), 109278.

Kidder, D.L., Erwin, D.H., 2001. Secular distribution of biogenic silica through the phanerozoic: comparison of silica replaced fossils and bedded cherts at the series level. Geology 109 (4), 509–522.

LaGrange, M.T., Konhauser, K.O., Catuneanu, O., Harris, B.S., Playter, T.L., Gingras, M. K., 2020. Sequence stratigraphy in organic-rich marine mudstone successions using chemostratigraphic datasets. Earth Sci. Rev. 203 (16), 103137.

Lan, Z.W., 2022. WANCE: a possibly volcanism-induced ediacaran carbon isotope excursion. J. Earth Sci. 33 (3), 778–788.

Lash, G.G., Blood, D.R., 2014. Organic matter accumulation, redox, and diagenetic history of the Marcellus Formation, southwestern Pennsylvania, Appalachian basin. Mar. Petrol. Geol. 57, 244–263.

Li, Y.F., Zhang, T.W., Ellis, G.S., Shao, D.Y., 2017. Depositional environment and organic matter accumulation of upper ordovician-lower Silurian marine shale in the upper Yangtze platform, South China. Palaeogeogr. Palaeoclimatol. Palaeoecol. 466, 252–264.

Lin, L.B., Yu, Y., Zhai, C.B., Li, Y.H., Wang, Y.N., Liu, G.X., Guo, Y., Gao, J., 2018. Paleogeography and shale development characteristics of the late permian longtan Formation in southeastern Sichuan Basin, China. Mar. Petrol. Geol. 95, 67–81.

Liu, B., Song, Y., Zhu, K., Su, P., Ye, X., Zhao, W., 2020. Mineralogy and element geochemistry of salinized lacustrine organic-higher shale in the Middle Permian Santanghu Basin: implications for paleoenvironment, provenance, tectonic setting and shale oil potential. Mar. Petrol. Geol. 120, 104569.

Liu, C., Jarochowska, E., Du, Y., Vachard, D., Munnecke, A., 2015. Microfacies and carbon isotope records of Mississippian carbonates from the isolated Bama Platform of Youjiang Basin, South China: possible responses to climate-driven upwelling. Palaeogeogr. Palaeoclimatol. Palaeoecol. 438, 96–112.

Liu, S.G., Yang, Y., Deng, B., Zhong, Y., Wen, L., Sun, W., Li, Z.W., Jansa, L.B., Li, J.X., Song, J.M., Zhang, X.H., Peng, H.L., 2021. Tectonic evolution of the Sichuan basin, southwest China. Earth Sci. Rev. 213, 103470.

Liu, Z.X., Yan, D.T., Niu, X., 2023. Pyrite concretions in the lower cambrian Niutitang formation, South China: response to hydrothermal activity. J. Earth Sci. 34 (4), 1053–1067.

Lu, J.F., Qie, W.K., Chen, X.Q., 2016. Pragian and lower emsian (lower devonian) conodonts from liujing, Guangxi, South China. Alcheringa 40, 275–296.

Luning, S., Craig, J., Loydell, D.K., Storch, P., Fitches, B., 2000. Lower Silurian 'hot shales' in North Africa and Arabia: regional distribution and depositional model. Earth Sci. Rev. 49, 121–200.

Ma, Y.Q., Fan, M.J., Lu, Y.C., Guo, X.S., Hu, H.Y., Chen, L., Wang, C., Liu, X.C., 2016. Geochemistry and sedimentology of the Lower Silurian Longmaxi mudstone in southwestern China: implications for depositional controls on organic matter accumulation. Mar. Petrol. Geol. 75, 291–309.

Ma, Y.S., Chen, H.D., Wang, G.L., 2009a. Atlas of Tectonic-Sequence Lithofacies Paleogeography in South China. Science Press, Beijing.

Ma, X.P., Liao, W.H., Wang, D.M., 2009b. The Devonian System of China, with a discussion on sea-level change in South China. Geol. Soc., London, Special Pub. 314 (1), 241–262.

Mansour, A., Adeyilola, A., Gentzis, T., Carvajal-Ortiz, H., Zakharova, N., 2022. Depositional setting and organic matter characterization of the upper devonian antrim shale, Michigan basin: implications for hydrocarbon potential. Mar. Petrol. Geol. 140, 105683.

McGhee Jr., G.R., Clapham, M.E., Sheehan, P.M., Bottjer, D.J., Droser, M., 2013. A new ecological-severity ranking of major Phanerozoic biodiversity crises. Palaeogeogr. Palaeoclimatol. Palaeoecol. 370, 260–270.

Mei, M.X., Maurice E, T., Wang, Y., Liu, M., 2013. Facies-succession and architecture of the third-order sequences and their stratigraphic framework of the Devonian in Yunnan-Guizhou-Guangxi area, South China. J. Palaeogeogr. 2, 93–108.

Middelburg, J.J., Ch, van der Weijden, J.R.W., 1988. Woittiez Chemical processes affecting the mobility of major, minor and trace elements during weathering of granitic rocks. Chem. Geol. 68 (3-4), 253–273.

Parrish, J.T., 1982. Upwelling and petroleum source beds, with reference to paleozoic. AAPG (Am. Assoc. Pet. Geol.) Bull. 66 (6), 750–774.

Perry, K.A., Pedersen, T.F., 1993. Sulphur speciation and pyrite formation in meromictic ex-fjords. Geochem. Cosmochim. Acta 57, 4405–4418.

Playter, T.L., Konhauser, K.O., Hodgson, C.A., Owttrim, G., Mloszewska, A., Sutherland, B., Bekker, A., Zonneveld, J.-P., Pemberton, S.G., Gingras, M.K., 2017. Microbe-clay interactions as a mechanism for the preservation of organic matter and trace metal biosignatures in black shales. Chem. Geol. 459, 75–90.

Qie, W.K., Ma, X.P., Xu, H.H., Qiao, L., Liang, K., Guo, W., Song, J.J., Chen, B., Lu, J.F., 2019. Devonian integrative stratigraphy and timescale of China. Sci. China Earth Sci. 62, 112–134.
Raiswell, R., Berner, R.A., 1985. Pyrite formation in euxinic and semi-euxinic sediments. Am. J. Sci. 285, 710–724.
Raiswell, R., Berner, R.A., 1986. Pyrite and organic matter in Phanerozoic normal marine shales. Geochem. Cosmochim. Acta 50, 1967–1976.
Raiswell, R., Buckley, F., Berner, R.A., Anderson, T.F., 1988. Degree of pyritization of iron as a paleoenvironmental indicator of bottom-water oxygenation. J. Sediment. Petrol. 58, 812–819.
Rimmer, S.M., 2004. Geochemical paleoredox indicators in Devonian-Mississippian black shales, central Appalachian Basin (USA). Chem. Geol. 206 (3-4), 373–391.
Ross, D.J.K., Bustin, R.M., 2009. Investigating the use of sedimentary geochemical proxies for paleoenvironment interpretation of thermally mature organic-rich strata: examples from the Devonian-Mississippian shales, Western Canadian Sedimentary Basin. Chem. Geol. 260, 1–19.
Rowe, H.D., Loucks, R.G., Ruppel, S.C., Rimmer, S.M., 2008. Mississippian barnett formation, fort worth basin, Texas: bulk geochemical inferences and Mo-TOC constraints on the severity of hydrographic restriction. Chem. Geol. 257 (1-2), 16–25.
Sageman, B.B., Murphy, A.E., Werne, J.P., Ver Straeten, C.A., Hollander, D.J., Lyons, T. W., 2003. A tale of shales: the relative roles of production, decomposition, and dilution in the accumulation of organic-rich strata, Middle-Upper Devonian, Appalachian basin. Chem. Geol. 195 (1-4), 229–273.
Schoepfer, S.D., Shen, J., Wei, H.Y., Tyson, R.V., Ingall, E., Algeo, T.J., 2015. Total organic carbon, organic phosphorus, and biogenic barium fluxes as proxies for paleomarine productivity. Earth Sci. Rev. 149, 23–52.
Scholz, F., Hensen, C., Noffke, A., Rohde, A., Liebetrau, V., Wallmann, K., 2011. Early diagenesis of redox-sensitive trace metals in the Peru upwelling area – response to ENSO-related oxygen fluctuations in the water column. Geochem. Cosmochim. Acta 75 (22), 7257–7276.
Scotese, C.R., 2001. Digital paleogeographic map archive on CD-ROM. In: PALEOMAP Project. University of Texas, Arlington. http://www.scotese.com (PALEOMAP website).
Scotese, C.R., McKerrow, W.S., 1990. Revised World maps and introduction. Palaeogeography and Biogeography 12, 1–21. Geological Society Memoir.
Shao, T.B., Zhou, Y., Cai, Y.F., Liang, X.Q., Song, M.S., 2020. Detrital zircon U-Pb ages and Hf isotopes of Lower-Middle Devonian to Middle Jurassic sandstones in the Qinfang basin, southern South China block: constraints on provenance and tectonic setting. J. Asian Earth Sci. 204, 104578.
Singh, P., 2008. Lithofacies and Sequence Stratigraphic Framework of the Barnett Shale, Northeast Texas. University of Oklahoms, Norman, p. 181.
Skei, J., 1983. Geochemical and sedimentological considerations of a permanently anoxic fjord-Framvaren, south Norway. Sediment. Geol. 36 (2-4), 131–145.
Sweere, T., van den Boorn, S., Dickson, A.J., Reichart, G.J., 2016. Definition of new trace-metal proxies for the controls on organic matter enrichment in marine sediments based on Mn, Co, Mo and Cd concentrations. Chem. Geol. 441, 235–245.
Tang, L., Song, Y., Jiang, S., Jiang, Z.X., Li, Z., Yang, Y.D., Li, X.H., Xiao, L., 2020. Organic matter accumulation of the Wufeng-Longmaxi shales in southern Sichuan Basin: evidence and insight from volcanism. Mar. Petrol. Geol. 120, 104564.
Taylor, S.R., Mclennan, S.M., 1985. The Continental Crust: its Composition and Evolution. Blackwell, London.
Tribovillard, N., Algeo, T.J., Baudin, F., Riboulleau, A., 2012. Analysis of marine environmental conditions based on molybdenum-uranium covariation-Applications to Mesozoic paleoceanography. Chem. Geol. 324–325, 46–58.
Tribovillard, N., Algeo, T.J., Lyons, T., Riboulleau, A., 2006. Trace metals as paleoredox and paleoproductivity proxies: an update. Chem. Geol. 232, 12–32.
Tyson, R.V., 1995. Sedimentary organic matter. In: Tyson, R.V. (Ed.), Organic Facies and Palynofacies. Chapman and Hall, London.
Walliser, O.H., 1996. Global events in the devonian and carboniferous. In: Walliser, O.H. (Ed.), Global Events and Event Stratigraphy in the Phanerozoic. Springer-Verlag, Berlin, pp. 225–250.
Wang, Q., Groves, D., 2018. Carlin-style gold deposits, Youjiang Basin, China: tectono-thermal and structural analogues of the Carlin-type gold deposits, Nevada, USA. Miner. Deposita 53, 909–918.
Wang, R., Shi, W.Z., Xie, X.Y., Wang, L.L., Busbey, A.B., Manger, W., Xia, Z.M., 2017. Hydrothermal indications of early cretaceous red beds in lacustrine successions, north yellow sea basin, eastern China. Mar. Petrol. Geol. 88, 739–755.
Wang, Y.X., Xu, S., Hao, F., Lu, Y.B., Shu, Z.G., Yan, D.T., Lu, Y.C., 2019. Geochemical and petrographic characteristics of Wufeng-Longmaxi shales, Jiaoshiba area, southwest China: implications for organic matter differential accumulation. Mar. Petrol. Geol. 102, 138–154.
Wei, H., Feng, Q.L., Yu, J.X., Chang, S., 2022. Characteristics and sources of organic matter from the early cambrian Niutitang formtion and its preservation environment in Guizhou. J. Earth Sci. 33 (4), 933–944.
Wignall, P.B., Bond, D.P.G., Kuwahara, K., Kakuwa, Y., Newton, R.J., Poulton, S.W., 2010. An 80-million-year oceanic redox history from Permian to Jurassic pelagic sediments of the Mino-Tamba terrane, SW Japan, and the origin of four mass extinctions. Global Planet 71, 109–123.
Wilkin, R.T., Barnes, H.L., Brantley, S.L., 1996. The size distribution of framboidal pyrite in modern sediments: an indicator of redox conditions. Geochem. Cosmochim. Acta 60 (20), 3897–3912.
Wilkin, R.T., Barnes, H.L., Brantley, S.L., 1997. Formation processes of framboidal pyrite. Geochem. Cosmochim. Acta 61, 323–339.
Wu, L.Y., Hu, D.F., Lu, Y.C., Liu, R.B., Liu, X.F., 2016. Advantageous shale lithofacies of Wufeng formation-longmaxi Formation in fuling gas field of Sichuan Basin, SW China. Petrol. Explor. Dev. 43, 208–217.
Wu, Y.W., Tian, H., Gong, D.J., Li, T.F., Zhou, Q., 2020. Paleo-environmental variation and its control on organic matter enrichment of black shales from shallow shelf to slope regions on the Upper Yangtze Platform during Cambrian Stage 3. Palaeogeogr. Palaeoclimatol. Palaeoecol. 545, 109653.
Wu, Z.R., He, S., He, Z.L., Li, X.C., Zhai, G.Y., Huang, Z.Q., 2022. Petrographical and geochemical characterization of the Upper Permian Longtan formation and Dalong Formation in the Lower Yangtze region, South China: implications for provenance, paleoclimate, paleoenvironment and organic matter accumulation mechanisms. Mar. Petrol. Geol. 139, 105580.
Xiao, B., Liu, S.G., Li, Z.W., Ran, B., Ye, Y.H., Yang, D., Li, J.X., 2021. Geochemical characteristics of marine shale in the Wufeng Formation-Longmaxi Formation in the northern Sichuan Basin, South China and its implications for depositional controls on organic matter. J. Petrol. Sci. Eng. 203, 108618.
Xu, H.Y., Hou, D.J., Löhr, S.C., Liu, Q.Y., Jin, Z.J., Shi, J.Y., Liang, X.P., Niu, C.K., George, S.C., 2023. Millimetre-scale biomarker heterogeneity in lacustrine shale identifies the nature of signal-averaging and demonstrates anaerobic respiration control on organic matter preservation and dolomitization. Geochem. Cosmochim. Acta 348, 107–121.
Yang, J., Du, Y.S., Huang, H., Yang, J.H., Huang, H.W., Huang, Z.Q., 2023. Devonian-carboniferous pillow OIB-type basalts in the Youjiang Basin, SW China: implications for the eastern extension of the paleo-tethys branch ocean. J. Earth Sci. 34 (3), 690–705.
Yang, L., Deng, J., Groves, D.I., Wang, Q.F., Zhang, L., Wu, W., Qin, K., Zhang, Q.Z., 2020. Recognition of two contrasting structural- and mineralogical-gold mineral systems in the Youjiang basin, China-Vietnam: orogenic gold in the south and Carlin-type in the North. Geosci. Front. 11, 1477–1494.
Yu, C.M., Li, Y., Liang, K., 2021. Devonian reef development and strata-bound ore deposits in South China. J. Palaeogeogr. 10 (4), 571–583.
Yu, C.M., Qie, W.K., Lu, J.F., 2018. Emsian (early devonian) Yujiang event in South China. Palaeoworld 27, 53–65.
Yuan, K., Huang, W.H., Fang, X.X., Li, S.Z., Wang, T., Lin, T., Liu, G.H., 2020. Geochemical characteristics and sedimentary environment of the middle devonian organic-higher shales in the Northwest of guizhong depression, southwest China. China Geology 3, 567–574.
Zeng, Y.F., Liu, W.J., Cheng, H.D., Zheng, R.C., Zhang, J.Q., Li, X.Q., Jiang, T.C., 1995. Evolution of sedimentation and tectonics of the Youjiang composite basin, South China. Acta Geologica Sinica-English Edition 8 (4), 358–371.
Zhang, G.Y., Tong, X.G., Xin, R.C., Wen, Z.X., Ma, F., Huang, T.F., Wang, Z.M., Yu, B.S., Li, Y.J., Chen, H.L., Liu, X.B., Liu, Z.D., 2019. Evolution of lithofacies and paleogeography and hydrocarbon distribution worldwide (I). Petrol. Explor. Dev. 46, 664–686.
Zhong, N.N., Lu, S.F., Huang, Z.L., Zhang, Y.S., 2004. TOC changes in the process of thermal evolution of source rock and its controls. Sci. China 47 (S2), 141–149.
Zou, C.N., Qiu, Z., Poulton, S.W., Dong, D.Z., Wang, H.Y., Chen, D.Z., Lu, B., Shi, Z.S., Tao, H.F., 2018. Ocean euxinia and climate change "double whammy" drove the Late Ordovician mass extinction. Geology 46, 535–538.